1   **Host specific sensing of coronaviruses and picornaviruses by the CARD8 inflammasome**

2

3   **Authors**

4   Brian V. Tsu[1], Rimjhim Agarwal[1], Nandan S. Gokhale[3], Jessie Kulsuptrakul[4], Andrew P. Ryan[1],

5   Lennice K. Castro[1], Christopher M. Beierschmitt[1], Elizabeth A. Turcotte[5], Elizabeth J. Fay[1],

6   Russell E. Vance[5,6], Jennifer L. Hyde[2], Ram Savan[3], Patrick S. Mitchell[2*], Matthew D.

7   Daugherty[1*]

8

9   **Affiliations:**

10   [1]Department of Molecular Biology, University of California, San Diego; La Jolla, CA, USA.

11   [2]Department of Microbiology, University of Washington; Seattle, WA, USA.

12   [3]Department of Immunology, University of Washington; Seattle, WA, USA.

13   [4]Molecular and Cellular Biology Graduate Program, University of Washington; Seattle, WA,

14   USA.

15   [5]Division of Immunology and Pathogenesis, University of California, Berkeley; Berkeley, CA,

16   USA.

17   [6]Howard Hughes Medical Institute, University of California, Berkeley; Berkeley, CA, USA.

18

19   *Corresponding authors. Matthew D. Daugherty (mddaugherty@ucsd.edu) and Patrick S.

20   Mitchell (psmitche@uw.edu)

21

22   **Short title: Coronavirus and picornavirus proteases activate the CARD8 inflammasome**

23

24   **Keywords: Host-virus evolution, CARD8, inflammasome, effector-triggered immunity,**

25   **viral proteases, coronaviruses, picornaviruses, SARS-CoV-2, COVID-19**

26

27   **Abstract**

28   Hosts have evolved diverse strategies to respond to microbial infections, including the detection

29   of pathogen-encoded proteases by inflammasome-forming sensors such as NLRP1 and CARD8.

30   Here, we find that the 3CL protease (3CL^{pro}) encoded by diverse coronaviruses, including

31   SARS-CoV-2, cleaves a rapidly evolving region of human CARD8 and activates a robust

32   inflammasome response. CARD8 is required for cell death and the release of pro-inflammatory

33   cytokines during SARS-CoV-2 infection. We further find that natural variation alters CARD8

34   sensing of 3CL^{pro}, including 3CL^{pro}-mediated antagonism rather than activation of megabat

35   CARD8. Likewise, we find that a single nucleotide polymorphism (SNP) in humans reduces

36   CARD8's ability to sense coronavirus 3CL^{pros}, and instead enables sensing of 3C proteases

37   (3C^{pro}) from select picornaviruses. Our findings demonstrate that CARD8 is a broad sensor of

38   viral protease activities and suggests that CARD8 diversity contributes to inter- and intra-species

39   variation in inflammasome-mediated viral sensing and immunopathology.

Introduction

Effector-triggered immunity (ETI) is a host defense strategy by which innate immune sensors

recognize pathogens via the detection of pathogen-specific activities (*1-5*). A subset of

eukaryotic ETI sensors form inflammasomes—large, intracellular immune complexes that

activates a pro-inflammatory caspase, predominantly caspase-1 (CASP1), to initiate

inflammatory signaling via interleukin (IL)-1β and IL-18 and pyroptotic cell death through

cleavage of the pore-forming protein Gasdermin D (GSDMD) (*6-8*). In humans, the activity of

viral proteases can be sensed by the inflammasome-forming sensors CARD8 and NLRP1 (*9-12*).

CARD8 is comprised of a disordered N-terminal region and a C-terminal function-to-fund

domain (FIIND) and caspase activation and recruitment domain (CARD). The FIIND undergoes

self-cleavage resulting in a bipartite sensor, with the disordered N-terminus acting as a 'tripwire'

for viral proteases. For instance, proteolytic cleavage of CARD8 by the HIV-1 protease (HIV-

1^{pro}) leads to proteasome-dependent 'functional degradation' (*13, 14*) of the cleaved N-terminus

and release of the bioactive CARD-containing C-terminus, which is sufficient for inflammasome

assembly and activation (*12*). However, the extent to which CARD8 has evolved to sense other

viral proteases and functions as an innate immune sensor of viral infection has been unclear.

The SARS-CoV-2 3CL^{pro} activates the human CARD8 inflammasome via proteolysis

within the disordered N-terminus

To determine if the CARD8 inflammasome can sense coronavirus infection by mimicking sites

of viral polyprotein cleavage, we expanded our previous bioinformatic approach (*11*) to generate

a predictive model for the *Coronaviridae* main protease (3CL^{pro}, also known as nsp5 or M

protease), which has been shown to cleave host proteins in addition to the coronavirus

3

63 polyprotein (*15-19*). The resulting 3CL^{pro} cleavage motif, XXΦQ[G/A/S]XXX (where Φ denotes

64 a hydrophobic residue and X denotes any amino acid) (**Fig 1A, S1 Fig, S1 and S2 Tables**) is

65 broadly consistent with previous studies (*20-23*), and allowed us to predict two putative 3CL^{pro}

66 cleavage sites within the N-terminus of human CARD8 (**Fig 1A**).

67

68 To determine if human CARD8 is cleaved by coronavirus 3CL^{pro}, we co-expressed an N-

69 terminal 3xFlag/mCherry-tagged isoform of human CARD8 (wild-type (WT)) with 3CL^{pro} from

70 SARS-CoV-2 in HEK293T cells (**Fig 1B and S2 Fig**). We used HIV-1^{pro} as a positive control

71 since it had previously been shown to cleave CARD8 between residues F59-F60 (site F59 in **Fig**

72 **1, A and B**). We observed a ~34kDa CARD8 product in the presence of SARS-CoV-2 3CL^{pro}

73 but not the catalytically inactive C145A 3CL^{pro} mutant. The ~34kDa product is predicted to

74 result from cleavage at site Q37 (**Fig 1A**), which migrated slightly below the cleavage product of

75 HIV-1^{pro}. Mutating the putative P1 residue in the Q37 site (CARD8 Q37A) eliminated the 34kDa

76 product, confirming SARS-CoV-2 3CL^{pro} cleavage at this site. The CARD8 Q37A mutant also

77 revealed a cryptic ~37kDa 3CL^{pro}-dependent product, which matches cleavage at the predicted

78 site Q61 (**Fig 1A and S2 Fig**). The CARD8 Q37A Q61A mutant was completely insensitive to

79 cleavage by SARS-CoV-2 3CL^{pro} (**Fig 1B**), whereas cleavage by the HIV-1^{pro} was unperturbed

80 by either mutant. Thus, CARD8 can be cleaved by SARS-CoV-2 3CL^{pro} at amino acid sequences

81 that mimic the coronavirus polyprotein cleavage site.

82

83 For both NLRP1 and CARD8, N-terminal proteolytic cleavage can activate CASP1 in a

84 reconstituted inflammasome assay (*10-12, 14, 24*). Consistent with the prior observation that

85 CARD8 is endogenously expressed in some HEK293T cell lines (*12*), transfection of our

86
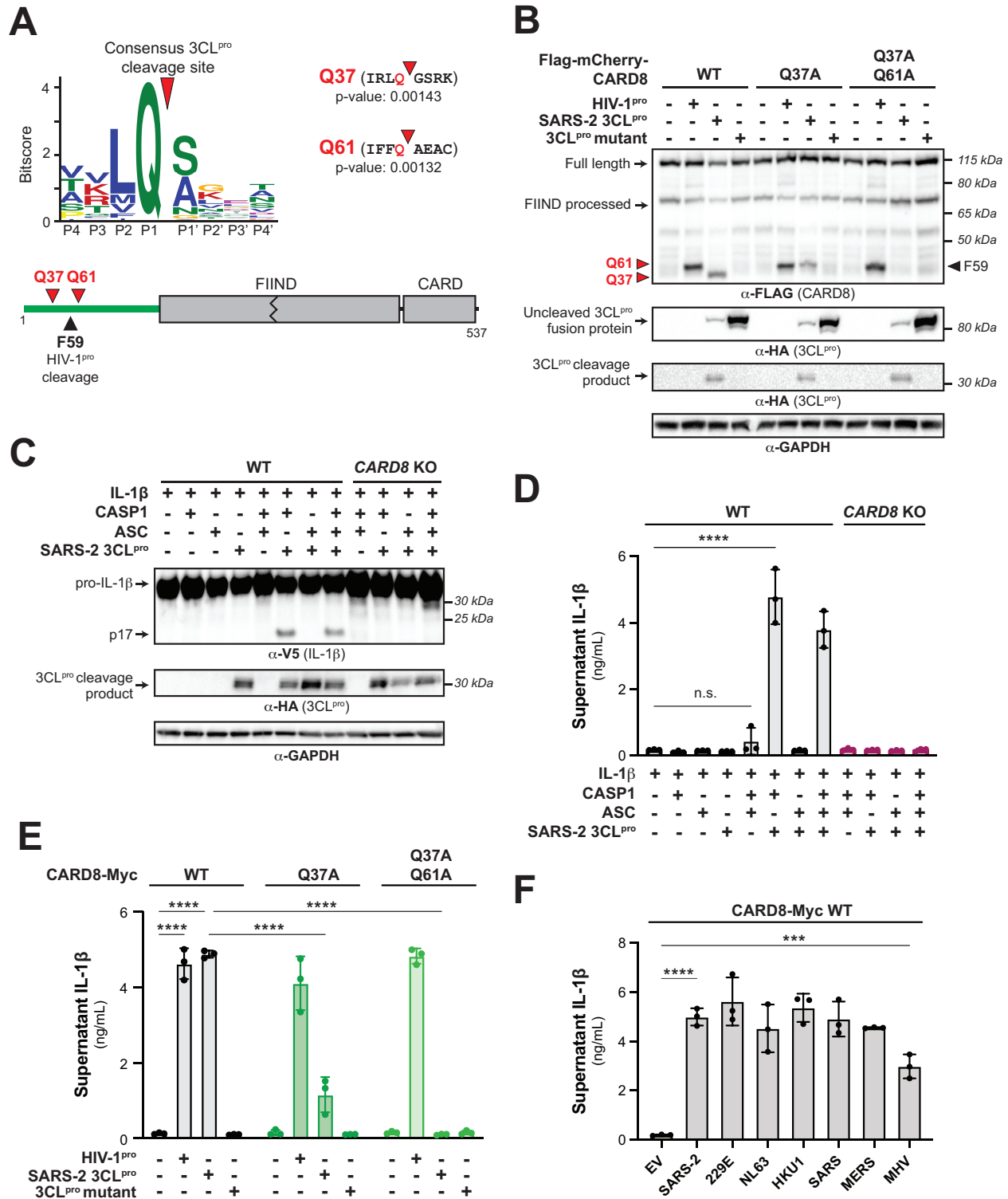
Fig 1. 3CL^{pro} from SARS-CoV-2 and other coronaviruses cleaves and activates the human CARD8 inflammasome. (A) A consensus betacoronavirus 3CL^{pro} cleavage motif (*upper* panel, Fig S1 and Methods) was used to predict two 3CL^{pro} cleavage sites (red triangles) within the disordered 'tripwire' N-terminus of human CARD8 (*lower* panel, green) near the described site

91   of HIV-1^{pro} cleavage (black triangle). Flanking residues and p-values of prediction for each site

92   (Q37 and Q61) are shown. (B) HEK293T cells were transfected with the indicated CARD8

93   construct in the presence ('+') or absence ('-') of indicated proteases. Active (SARS-2 3CL^{pro}) or

94   catalytically inactive (3CL^{pro} mutant) protease from SARS-CoV-2 was expressed as an HA-

95   tagged fusion construct (Fig S2). HIV-1^{pro} was expressed from an untagged gag-pol construct.

96   Triangles are as described in (A). (C-D) WT or *CARD8* KO HEK293T cells were transfected

97   with ('+') or without ('-') indicated constructs. Inflammasome activation was monitored by

98   immunoblotting for mature IL-1β (p17) (C) or measuring culture supernatant levels of bioactive

99   IL-1β using IL1R-expressing reporter cells (D). (E-F) *CARD8* KO HEK293T cells were co-

100   transfected with the indicated CARD8 and protease constructs and supernatant levels of

101   bioactive IL-1β were measured by IL1R reporter assay. 3CL^{pros} from the following viruses were

102   used: HCoV-229E (229E), HcoV-NL63 (NL63), HcoV-HKU1 (HKU1), SARS-CoV (SARS),

103   MERS-CoV (MERS), mouse hepatitis virus (MHV). (D-F) Individual values (n=3), averages,

104   and standard deviations shown are representative of experiments performed in triplicate. Data

105   were analyzed using two-way ANOVA with Šidák's post-test (D-E) or one-way ANOVA with

106   Tukey's post-test (F). *** = p<0.001, **** = p<0.0001, n.s. = not significant.

107

108   HEK293T cells with only CASP1, pro-IL-1β, and SARS-CoV-2 3CL^{pro} resulted in robust

109   CASP1-dependent processing of pro-IL-1β to mature bioactive IL-1β (p17) as measured by

110   immunoblot or IL-1β reporter assay (see **Methods**) (**Fig 1, C and D**). Inflammasome activation

111   was not observed in cells in *CARD8* knock out (KO) cells.

112

113   For both NLRP1 and CARD8, N-terminal proteolytic cleavage can activate CASP1 in a

114   reconstituted inflammasome assay (*10-12, 14, 24*). Validating a prior observation that CARD8 is

115   endogenously expressed in some HEK293T cell lines (*12*), transfection of our HEK293T cells

116   with CASP1, pro-IL-1β, and SARS-CoV-2 3CL^{pro} resulted in robust CASP1-dependent

117   processing of pro-IL-1β to mature bioactive IL-1β (p17) as measured by immunoblot or IL-1β

118   reporter assay (**Fig 1, C and D**). We found that inflammasome activation was CARD8-

119   dependent since we did not observe CASP1-processed IL-1β in HEK293T *CARD8* knock out

120   (KO) cells. To confirm that SARS-CoV-2 3CL^{pro} cleavage of CARD8 is responsible for

121   inflammasome activation, we complemented *CARD8* KO cells with WT CARD8 or cleavage site

122   mutants. Complementation with WT CARD8 rescued both HIV-1^{pro} and 3CL^{pro}-induced

123   inflammasome activation (**Fig 1E and S3 Fig**). In contrast, whereas CARD8 cleavage site

124   mutants had no effect on HIV-1^{pro}-induced inflammasome activation, 3CL^{pro}-induced

125   inflammasome activation was reduced or abolished in *CARD8* KO cells complemented with

126   CARD8 Q37A or CARD8 Q37A Q61A, respectively (**Fig 1E and S3 Fig**). These results validate

127   that 3CL^{pro} site-specific cleavage is required for CARD8 inflammasome activation. As expected,

128   3CL^{pro} inflammasome activation did not occur in *CARD8* KO cells complemented with the

129   CARD8 FIIND auto-processing mutant S297A mutant (**S4 Fig**) (*12, 25, 26*). Taken together, our

130   results indicate that human CARD8 senses the proteolytic activity of the SARS-CoV-2 3CL^{pro},

131   which drives inflammasome activation via functional degradation.

132

133   To test if proteases from other coronaviruses also cleave CARD8, we cloned 3CL^{pros} from other

134   human-relevant beta-coronaviruses (SARS-CoV (SARS), MERS-CoV (MERS), HCoV-HKU1

135   (HKU1), two human alpha-coronaviruses (HCoV-229E (229E) and HCoV-NL63 (NL63), and

136   the mouse beta-coronavirus murine hepatitis virus (MHV) (**S5 Fig**). Consistent with their

137   structural and cleavage motif similarity (*27*), we found that every tested 3CL^{pro} was able to

138   cleave and activate CARD8 in a site-specific manner (**Fig 1F and S6 Fig**). Thus, effector-

139   triggered immunity by human CARD8 is a conserved pathway for sensing of both endemic and

140   pandemic human coronaviruses.

141

142   **Coronavirus infection activates the CARD8 inflammasome**

143   We next evaluated the consequences of CARD8 inflammasome activation by infecting the

144   human monocyte-like cell line THP-1 with HCoV-229E. We found that HCoV-229E infected

145   WT but not two independently-derived *CARD8* KO THP-1 cell lines underwent significant cell

146   death (**Fig 2A**) and release of IL-1β (**Fig 2B**), a result similar to treatment with Val-boroPro

147   (VbP), which specifically activates the CARD8 inflammasome in myeloid and lymphoid

148   lineages (*26, 28*) (**S7 Fig**). SARS-CoV-2 infection (*29, 30*) or uptake via FcyR-mediated

149   antibody-dependent enhancement (*31*) by monocytes or macrophages induces inflammasome

150   activation. To determine if CARD8 senses and responds to SARS-CoV-2 infection in THP-1

151   cells, we engineered WT or *CARD8* KO THP-1 cells to express ACE2 and TMPRSS2 (THP-

152   1^{A+T}). As with HCoV-229E, we found that SARS-CoV-2 infection of THP-1^{A+T} WT but not
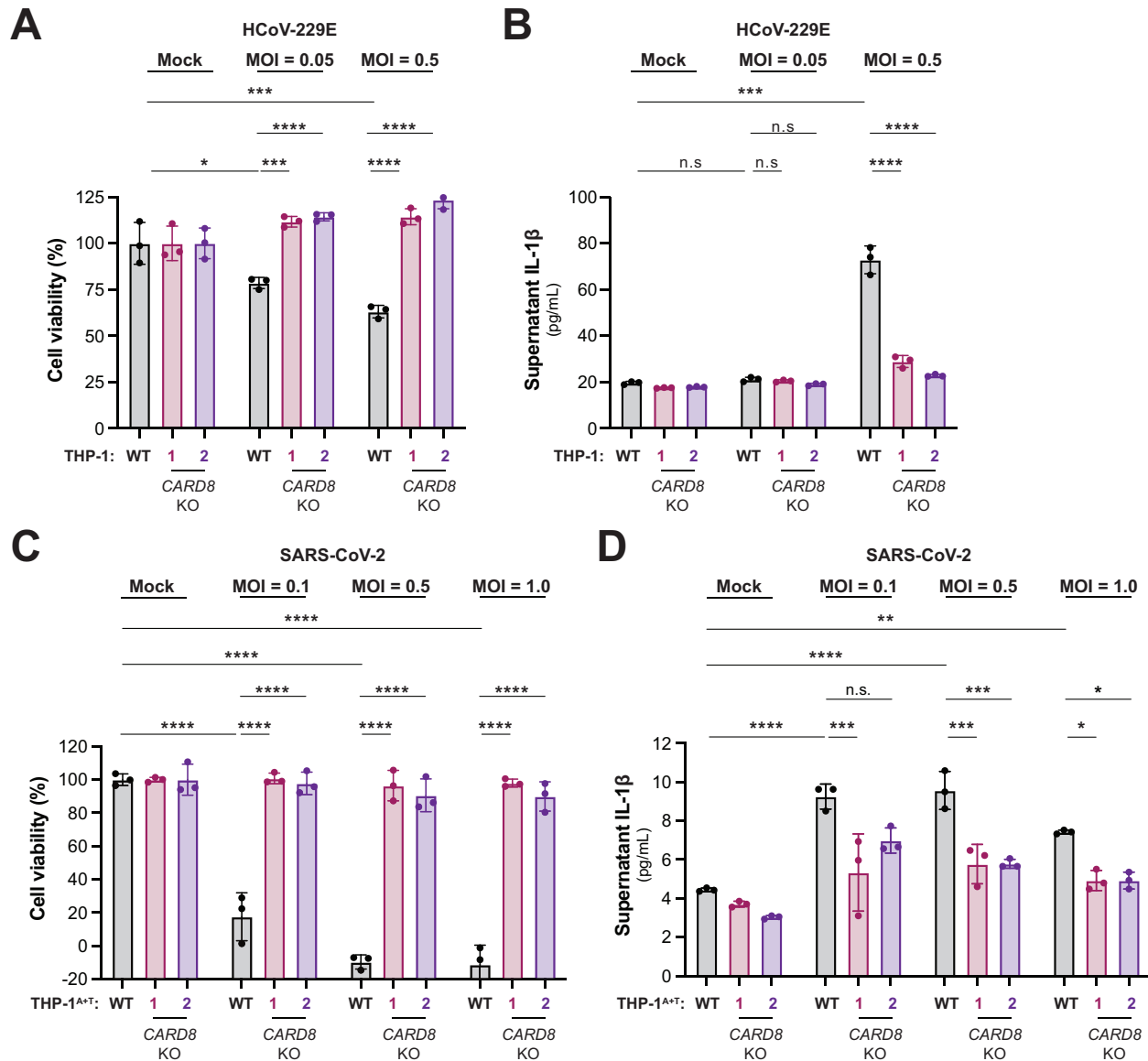
153

Fig 2. Coronavirus infection activates the CARD8 inflammasome in THP-1 cells. WT, *CARD8* KO1, and *CARD8* KO2 THP-1 cells (A-B) or THP-1 cells expressing ACE2 and TMPRSS2 (THP-1^{T+A}) (C- D) were primed with 0.5 µg/mL Pam3CSK4 for 6h, followed by infection with the coronaviruses hCoV-229E (A-B) or SARS-CoV-2 (SARS-2) (C-D) at the indicated multiplicity of infection (MOI). 48h post-infection, cell viability (A, C) was measured using the Cell Titer Glo assay and IL-1β levels were measured using the IL1R reporter assay (B, D) as in **Fig 1D**. Data presented are representative of experiments performed at least twice. Data were analyzed using two-way ANOVA with Šidák's post-test: * = p<0.05, ** = p<0.01, *** = p<0.001, **** = p<0.0001, n.s. = non-significant.

9

164   *CARD8* KO cells induced both cell death and IL-1β release (**Fig 2, C and D**). Our results

165   demonstrate that CARD8 is a bona fide innate immune sensor of viral infection.

166

167   **Inter- and intra-host diversity in CARD8 impacts inflammatory responses to coronavirus**

168   **proteases**

169   Host-virus interactions, including those between viral proteases and host cleavage targets, are

170   often engaged in evolutionary arms races that shape the specificity of host-virus interactions (*15,*

171   *32-34*). Indeed, we have previously shown that the CARD8 homolog and viral protease sensor,

172   NLRP1, has been duplicated and recurrently lost across mammalian evolution. *NLRP1* also has

173   strong signatures of positive selection in an N-terminal region of the protein that is cleaved by

174   pathogen-encoded proteases, which we refer to as the 'tripwire' region due to its role in virus

175   detection and subsequent inflammasome activation (*11, 24*). We thus predicted that *CARD8* may

176   have a similarly dynamic evolutionary history, and that host inter- and intraspecies variation

177   would underlie differences in CARD8 cleavage and inflammasome activation by coronavirus

178   3CL^{pros}.

179

180   We first found that both *CARD8* and *NLRP1* are each present in only certain mammalian

181   lineages, consistent with their dynamic roles in host defense as opposed to dedicated

182   housekeeping functions (**Fig 3A**). For instance, we found that within the order *Chiroptera* (bats),

183   microbats retain a *NLRP1* ortholog but have lost *CARD8*, whereas megabats have lost *NLRP1*

184   and only encode *CARD8*. Because bats serve as main reservoir hosts of emerging coronaviruses

185   (*35, 36*), but is missing from microbats, we tested if the CARD8 inflammasome could serve as a

186   sensor for 3CL^{pro} in the megabat species *Rousettus aegyptiacus*. Unlike human CARD8, the *R.*

10
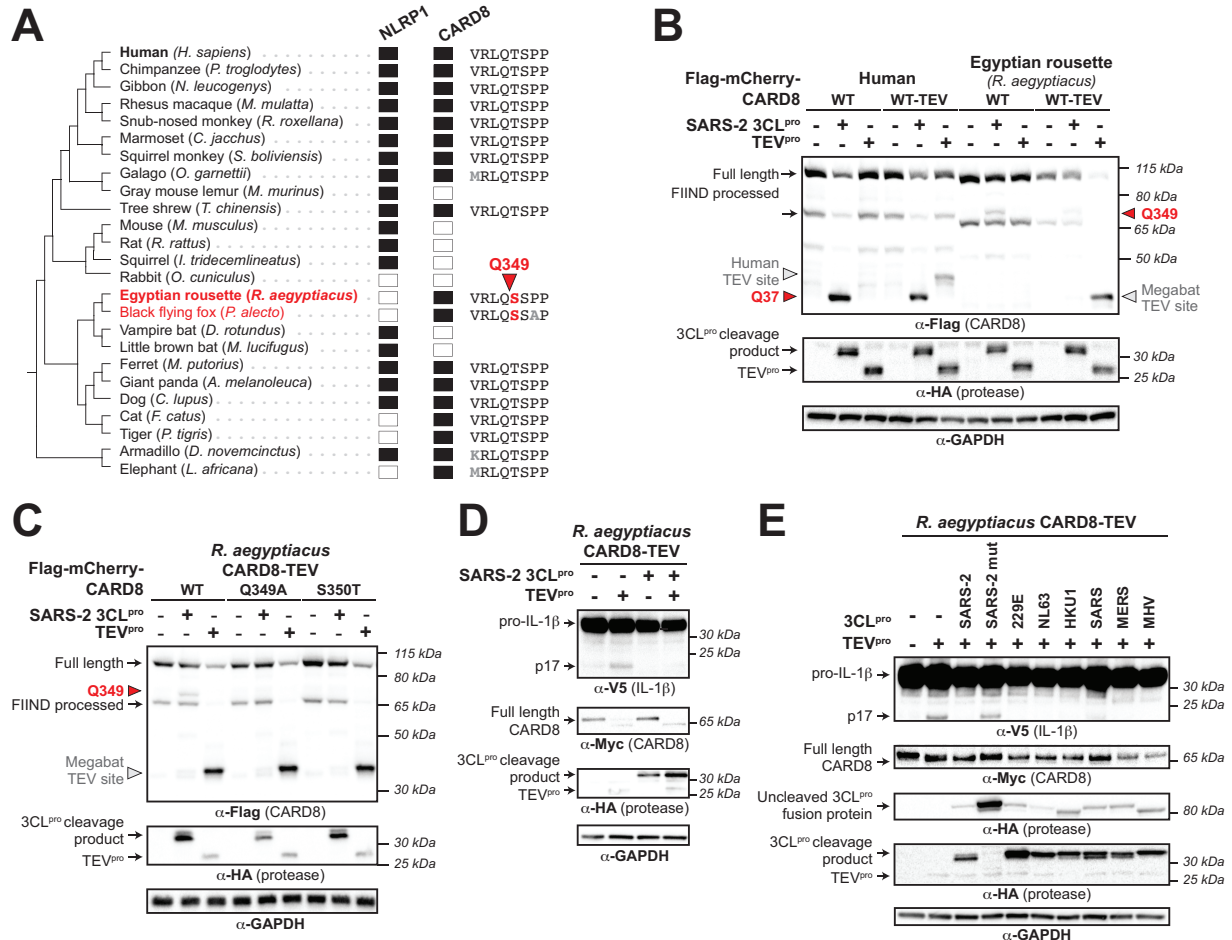
Fig 3. Megabat CARD8 is antagonized rather than activated by coronavirus 3CL^{pro}. (A) Presence (filled rectangle) or absence (empty rectangle) of predicted *NLRP1* or *CARD8* orthologs in the indicated mammalian species. To the left is a species phylogeny. Megabat species are indicated in red. To the right is an alignment of a predicted 3CL^{pro} cleavage site in *Rousettus aegyptiacus* CARD8 (red triangle indicates site and number indicates residue position). (B) Human CARD8 or *R. aegyptiacus* CARD8 was co-transfected with either SARS-CoV-2 (SARS-2) 3CL^{pro} or protease from tobacco etch virus (TEV^{pro}). For human or *R. aegyptiacus* CARD8 constructs labeled "WT-TEV", a TEV^{pro} site was introduced into the N-terminus. The red triangles and amino acid number indicates the sites of 3CL^{pro} cleavage in human and *R. aegyptiacus* CARD8. The gray triangles indicate the sites of TEV protease cleavage within each CARD8 WT-TEV. (C) Mapping of the 3CL^{pro} site within *R. aegyptiacus* CARD8 was performed by transfecting the indicated point mutants with SARS-CoV-2 (SARS-2) 3CL^{pro} or TEV^{pro}. 3CL^{pro} and TEV^{pro} sites are marked by triangles as in (B). (D) *CARD8* KO HEK293T cells were co-transfected with *R. aegyptiacus* IL-1β and CASP1, along with the indicated CARD8 and protease constructs. Presence of mature IL-1 β (p17) upon TEV^{pro} addition indicates successful reconstitution of the *R. aegyptiacus* CARD8 inflammasome, whereas absence of p17 upon SARS-2 3CL^{pro} indicates antagonism of the *R. aegyptiacus* CARD8 inflammasome. (E) *R. aegyptiacus* CARD8 inflammasome activation assays were performed as in (D) with the indicated 3CL^{pro} constructs.
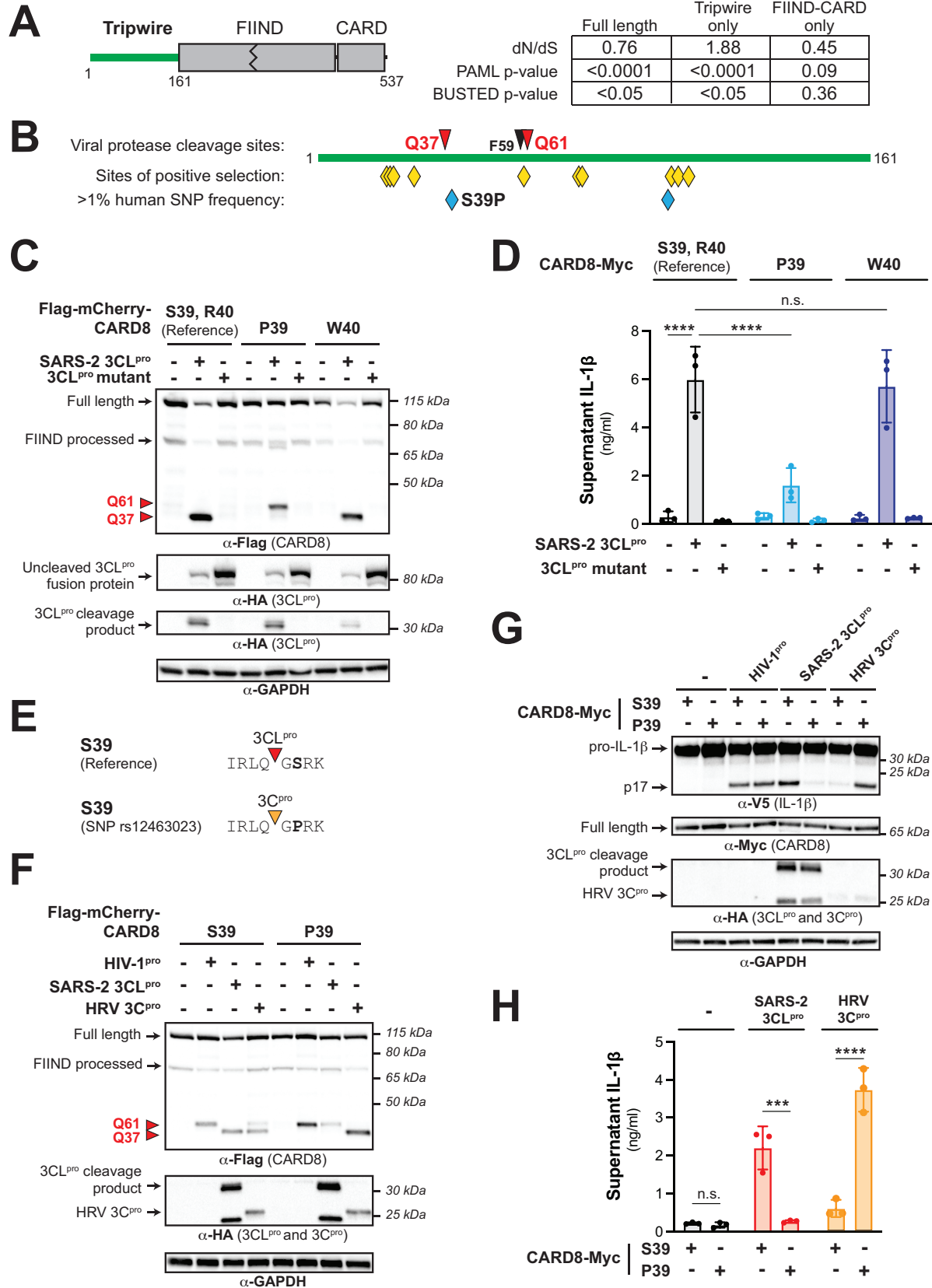
207   *aegyptiacus* CARD8 (CARD8$_{Ra}$) N-terminus lacks sites Q37 and Q61 and was not cleaved by

208   SARS-CoV-2 3CL^{pro}. We did, however, observe a cleavage product that matched a predicted

209   3CL^{pro} site at Q349 in CARD8$_{Ra}$ downstream of the FIIND auto-processing site in the

210   inflammasome-forming C-terminus (**Fig 3, A and B**). Interestingly, megabats are the only

211   mammals with a serine in the P1' position of the cleavage site (**Fig 3A and S8 Fig)**, which is

212   preferred for cleavage based on our computational model (**Fig 1A**). Indeed, a threonine in this

213   position (S350T), which is found in human CARD8 as well as most other mammals, prevents

214   cleavage of CARD8$_{Ra}$ by SARS-CoV-2 3CL^{pro} (**Fig 3C and S8 Fig**). We next wished to test the

215   functional effect of 3CL^{pro} on the megabat CARD8 inflammasome. First, we determined if

216   functional degradation could activate megabat CARD8 by inserting a TEV^{pro} cleavage site into

217   the N-terminus of CARD8$_{Ra}$, permitting TEV^{pro} cleavage of CARD8$_{Ra}$-TEV but not WT

218   CARD8$_{Ra}$. When co-expressed with CASP1 and pro-IL-1β from *R. aegyptiacus*, TEV^{pro}

219   cleavage of CARD8$_{Ra}$-TEV resulted in inflammasome activation, indicating that we can

220   reconstitute the *R. aegyptiacus* CARD8 inflammasome in human cells (**Fig 3D**). Using this

221   reconstitution system, we found that SARS-CoV-2 3CL^{pro} does not activate, and in fact

222   antagonizes TEV-mediated CARD8$_{Ra}$ inflammasome activation (**Fig 3D)**, similar to our previous

223   observations of viral proteases that antagonize the activation of the NLRP1 inflammasome (*11*).

224   We further found that all 3CL^{pros} that we tested can instead prevent TEV^{pro}-mediated activation

225   of the CARD8$_{Ra}$ inflammasome (**Fig 3E**). Together with the loss of CARD8 from many bat

226   species, these data provide a putative mechanism of disease tolerance that protects bats from

227   immunopathogenic effects of inflammasome activation.

228

229   We next focused on the evolution of human *CARD8*. Supporting a previous genome-wide study

230   (*37*), we found evidence that *CARD8* has evolved under recurrent positive selection in hominoids

231   and Old World monkeys, which we find is primarily driven by the N-terminal region of the

232   protein (**Fig 4A**). Codon-based analyses also show that positively selected sites are

233   predominantly found in the N-terminus, including a codon at position 60 that lies in the HIV-1^{pro}

234   site and the secondary coronavirus 3CL^{pro} site (**Fig 4B, S9 Fig, and S5 Table)**. We thus infer

235   that, like NLRP1, the CARD8 disordered N-terminus is a molecular 'tripwire' that is rapidly

236   evolving to mimic viral polyprotein sites and sense diverse viral proteases. We further analyzed

237   the human population for non-synonymous SNPs in *CARD8* (**Fig 4B**). Within the N-terminus,

238   we found several high frequency human SNPs, including a S39P variant that resides at the P2'

239   position within the 3CL^{pro} cleavage site and is present in >20% of all sampled African and

240   African American individuals (GnomAD v3.1.2 (*38*)) (**S9 Fig and S5 and S6 Tables**).

241   Strikingly, while CARD8 S39 and P39 variants are similarly cleaved and activated by HIV-1^{pro},

242   the CARD8 P39 variant exhibits reduced sensitivity to cleavage and activation by coronavirus

243   3CL^{pros} (**Fig 4, C and D, and S10 Fig**). This is reinforced by our observation that a proline in the

244   P2' position is never found in the >10,000 polyprotein cleavage sites we sampled from beta-

245   CoVs (**S1 Table**). In contrast, another human SNP (R40W) found in approximately 1 in every

246   2000 alleles (**S5 Table**), does not detectably affect CARD8 cleavage in our assays (**Fig 4, C and**

247   **D**). These data suggest that standing genetic variation in human CARD8 underlies differential

248   sensing and inflammasome responses to coronavirus infection.

249

250

13

A

Tripwire   FIIND   CARD

1   161   537

	Full length	Tripwire only	FIIND-CARD only
dN/dS	0.76	1.88	0.45
PAML p-value	<0.0001	<0.0001	0.09
BUSTED p-value	<0.05	<0.05	0.36

B

Viral protease cleavage sites: Q37   F59 Q61

Sites of positive selection:

>1% human SNP frequency: S39P

1   161

C

D

E

S39 (Reference)   3CLpro   IRLQ GSRK

S39 (SNP rs12463023)   3Cpro   IRLQ GPRK

F

G

H

251

14

Fig 4. Human polymorphism in CARD8 reduces sensing of coronavirus 3CL^{pro} while increasing sensing of select picornavirus 3C^{pros}. (A) Evolutionary analyses of positive selection were performed on full length *CARD8* (encoding residues 1-537), the disordered N-terminal 'tripwire' region (encoding residues 1-161), and the FIIND-CARD region (encoding residues 162-537). P-values from PAML and BUSTED analyses are shown, along with the dN/dS value obtained from PAML. (B) Schematic of the CARD8 'tripwire' region. Red and black triangles and amino acid numbers indicate sites of 3CL^{pro} and HIV-1^{pro} cleavage respectively. Yellow diamonds indicate codons predicted to be evolving under positive selection by at least one evolutionary analysis (table S4). Blue diamonds indicate high frequency (>1% allele frequency) non-synonymous single nucleotide polymorphisms (SNPs) in humans (table S5 and S6). The position of the S39P substitution that results from SNP rs12463023 is shown. (C-D) Reference human CARD8 (S39, R40) or human CARD8 variants (P39 or W40) were co-expressed with the indicated protease construct and assayed for 3CL^{pro}-mediated cleavage (C) or CARD8 inflammasome activation (D). (E) Amino acid sequence surrounding the Q37 cleavage site for S39 (reference) and P39 variants of human CARD8. Triangles mark sites of cleavage by the indicated viral protease (F-H). Human CARD8 S39 or CARD8 P39 were transfected with the indicated proteases and assayed for 3CL^{pro}-mediated cleavage (F) or CARD8 inflammasome-mediated maturation of IL-1β (G) or the release of bioactive IL-1β (H). HRV 3C^{pro} = human rhinovirus 3C^{pro}. Individual values (n=3), averages, and standard deviations shown are representative of experiments performed in triplicate. Data were analyzed using two-way ANOVA with Šidák's post-test. *** = p<0.001, **** = p<0.0001, n.s. = not significant.

15

273 **A human SNP confers a specificity switch for CARD8 sensing of coronavirus 3CL^pro and**

274 **human rhinovirus 3C^pro**

275 Finally, we considered if the CARD8 P39 variant, in addition to affecting sensing of coronavirus

276 3CL^pros, also alters recognition of other pathogens. We noticed that although a P2' proline is

277 disfavored in our model for 3CL^pro cleavage, a P2' proline is strongly preferred in our model for

278 enterovirus 3C^pro cleavage (*11*). Indeed, our 3C^pro motif search (*11*) identified a cleavage site in

279 CARD8 P39 but not CARD8 S39 (**Fig 4E and S11 Fig**). Validating these bioinformatic

280 predictions, cleavage assays with the 3C^pro from the respiratory picornavirus, human rhinovirus

281 (HRV), revealed that HRV 3C^pro cleavage of human CARD8 at site Q37 is considerably more

282 pronounced for the P39 variant than the S39 variant (**Fig 4F**). Likewise, we found that

283 inflammasome activation by HRV 3C^pro was nearly absent in HEK293T *CARD8* KO cells

284 complemented with CARD8 S39, whereas we observed robust inflammasome activation in cells

285 complemented with CARD8 P39 – the opposite sensitivity observed for SARS-CoV-2 3CL^pro

286 (**Fig 4, G and H**). Finally, we found that CARD8 variation also impacted cleavage by other

287 picornavirus 3C^pros. For example, 3C^pros from enterovirus D68 (EV68) and poliovirus (PV1) were

288 better sensed by CARD8 P39, whereas the Aichi virus 3C^pro was better sensed by the S39

289 CARD8 variant (**S12 Fig**). Thus, a single amino acid change in CARD8 functions as a viral-

290 specificity switch, underscoring the importance of pathogen-driven evolution in shaping

291 inflammasome responses.

292

293 **Discussion**

294 As is clear from the ongoing COVID-19 pandemic, understanding the molecular mechanisms

295 that drive viral sensing and inflammatory pathogenesis during infection remains key to

16

296 developing rationalized, host-directed treatments to support antiviral defense or quell severe

297 disease. CARD8 is expressed in airway epithelia (*10, 39, 40*) and other cell types, including

298 monocytes and T cells (*26, 28, 41*) that are physiologically relevant for respiratory coronaviruses

299 and picornaviruses (*39, 40, 42*), including SARS-CoV-2 (*29-31*). Our data showing that SARS-

300 CoV-2 infection activates the CARD8 inflammasome in THP-1 cells supports findings that

301 inflammasome activation contributes to severe COVID-19, and suggests that the CARD8

302 inflammasome in monocytes and macrophages contribute to inflammation in COVID-19

303 patients.

304

305 Based on our results and the finding that FcγR-mediated uptake of SARS-CoV-2 virions into

306 monocytes leads to abortive infection (*31*), we speculate that CARD8-dependent pyroptosis

307 contributes to the poor permissiveness of myeloid cells for SARS-CoV-2 (*43*), wherein the

308 myeloid compartment may not substantially contribute to viral load but likely impacts

309 immunopathology via inflammasome-driven inflammation (*44, 45*). Prior reports have proposed

310 a similar role for the NLRP3 inflammasome in myeloid cells (*29-31*). We favor a unifying model

311 in which CARD8-dependent GSDMD pore formation contributes to NLRP3 inflammasome

312 activation, which also offers an explanation for CARD8-dependent release of IL-1β (*46*).

313 Interestingly, the SARS-CoV-2 3CL^{pro} also cleaves and activates NLRP1 in airway epithelia (*9*).

314 This results in cell death via a non-canonical NLRP1>CASP8>CASP3>GSDME inflammasome

315 pathway, suggesting that the cellular context of inflammasome responses may uniquely shape

316 antiviral defense and/or inflammation. We also note that seasonal coronaviruses are capable of

317 activating CARD8, and we speculate that a multitude of variables such as cell tropism shape the

318 outcome of virus-induced inflammasome activation in antiviral immunity and pathogenesis.

319   Nevertheless, given the impact of SNPs on human CARD8 sensing of pathogenic viruses, it is

320   tempting to speculate that diminished CARD8 inflammasome activation may be a contributing

321   factor to variation in COVID-19 disease outcomes, and more generally for other human

322   pathogenic coronavirus and picornavirus infections. Further studies are required to establish this

323   connection.

324

325   Taken together, our findings establish CARD8 as a rapidly evolving, polymorphic, innate

326   immune sensor of infection by positive-sense RNA viruses. We demonstrate that CARD8 has the

327   capacity to detect viral proteases from at least three viral families that include important human

328   pathogens: *Coronaviridae, Picornaviridae,* and *Retroviridae*. These findings also build on the

329   emerging concept that ETI is an important mechanism of pathogen recognition, including the use

330   of host mimicry of viral polyprotein cleavage motifs as an evolutionary strategy in the ongoing

331   arms race between host and viruses.

332

333   **Materials and Methods**

334   *Motif generation and search*

335   To build the betacoronavirus (betaCoV) 3CL^{pro} cleavage motif, 995 nonredundant betaCoV

336   polyprotein sequences were collected from the Viral Pathogen Resource (ViPR) (*47*) and aligned

337   with five well-annotated reference enteroviral polyprotein sequences from RefSeq (**S1 Fig, A**

338   **and B**). P1 and P1' of the annotated cleavage sites across the RefSeq sequences served as

339   reference points for putative cleavage sites across the 995 ViPR sequences (**S1 Table**). Four

340   amino acid residues upstream (P4-P1) and downstream (P1'-P4') of each cleavage site were

341   extracted from every MAFFT-aligned (*48*) polyprotein sequence, resulting in 1000 sets of

342   cleavage sites (RefSeq sites included) (**S1 Table**). Each set of cleavage sites representative of

343   each polyprotein was then concatenated (**S2 Table**). Next, duplicates were removed from the

344   concatenated cleavage sites (**S2 Table**). The remaining 60 nonredundant, concatenated cleavage

345   sites were then split into individual 8-mer cleavage sites and were aligned using MAFFT (*48*) to

346   generate Geneious-defined (*49*) sequence logo information at each aligned position (**S2 Table**).

347   Pseudo-counts to the position-specific scoring matrix were adjusted as described previously (*11*)

348   and a motif p-value cut-off of 0.00231 corresponding to detection of 99% of the initial

349   polyprotein cleavage sites was selected (**S1 FigC**).

350

351   *Sequence alignments and phylogenetic trees*

352   Complete polyprotein sequences from 60 betaCoVs with non-redundant cleavage sites (see

353   'Motif generation and search' section above) were downloaded from ViPR. Sequences were

354   aligned using MAFFT (*48*) and a neighbor-joining phylogenetic tree was generated using

355   Geneious software (*49*).

356

357   *Evolutionary analyses*

358   For phylogenomic analyses of CARD8 and NLRP1 (**Fig 3A**), human CARD8 (accession

359   NP_001338711) and human NLRP1 (accession NP_127497.1) were used as BLASTP (*50*)

360   search queries against the indicated mammalian proteomes (**Fig 3A**). A species was determined

361   to have an ortholog if it had a protein with >50% sequence identity, >70% sequence coverage,

362   and was the bi-directional best hit to the indicated human protein. The species tree shown in **Fig**

363   **3A** is based on NCBI Common Tree

364   (https://www.ncbi.nlm.nih.gov/Taxonomy/CommonTree/wwwcmt.cgi). To identify regions of

365   mammalian CARD8s that are orthologous to the 3CL^pro cleavage site (Q349) in *Rousettus*

366   *aegyptiacus* CARD8, a 50 amino acid region of *R. aegyptiacus* CARD8 that was centered on the

367   Q349 cleavage site was used as a BLASTP query against the entire RefSeq protein database with

368   a 60% sequence identity cut-off. A single CARD8 sequence from each species (**S8 Fig)** was

369   aligned using MAFFT (*48*) and trimmed to only include the eight amino acid spanning the

370   cleavage site.

371   For positive selection analyses, primate nucleotide sequences that aligned to human full

372   length CARD8 (Protein: NP_001338711, mRNA: NM_001351782.2) were downloaded from

373   NCBI and aligned using MAFFT (*48*). Only eight other primate sequences, only from hominoids

374   and Old World monkeys, were fully alignable to full length human CARD8 (sequence accessions

375   in table S3). Maximum likelihood (ML) tests were performed with codeml in the PAML

376   software suite (*51*) or using BUSTED (*52*) on the DataMonkey (*53*) server. For PAML, aligned

377   sequences were subjected to ML tests using NS sites models disallowing (M7) or allowing (M8)

378   positive selection. The p-value reported is the result of a chi-squared test on twice the difference

379   of the log likelihood (lnL) values between the two models using two degrees of freedom. We

380   confirmed convergence of lnL values by performing each analysis using two starting omega

381   (dN/dS) values (0.4 and 1.5). Results are reported from analyses using the F61 codon frequency

382   model. Analyses with the F3x4 model gave similar results. For evolutionary analyses of regions

383   of CARD8, the full-length alignment was truncated to only include codons 1-161 ('tripwire'

384   region) or 162-537 (FIIND-CARD region) and PAML or BUSTED analyses were performed as

385   described above.

386   We used three independent methods to estimate individual codons within CARD8 that

387   have been subject to positive selection (**S4 Table**). PAML was used to identify positively

388   selected codons with a posterior probability greater than 0.90 using a Bayes Empirical Bayes

389   (BEB) analysis and the F61 or F3x4 codon frequency models. The same CARD8 alignment was

390   also used as input for FEL (*54*) and FUBAR (*55*) using the DataMonkey (*53*) server. In both

391   cases, default parameters were used and codons with a signature of positive selection with a p-

392   value of <0.1 are reported. In all cases, codon numbers correspond to the amino acid position and

393   residue in human CARD8 (NCBI accession NP_001338711).

394

395   *Plasmids and constructs*

396   Megabat CARD8, CASP1, IL-1β, and all 3CL^{pro} sequences were ordered as either gBlocks

397   (Integrated DNA Technologies, San Diego, CA) or Twist Gene Fragments (Twist Biosciences,

398   South San Francisco, CA). All sequences are found in **S7 Table**. Vectors containing the coding

399   sequences of human CARD8, ASC, human CASP1, human IL-1β-V5, and TEV^{pro} were

400   previously described (*24*). Vector psPAX2 containing the untagged coding sequence for HIV-1

401   gag-pol was a gift from Didier Trono (Addgene plasmid # 12260).

402   For CARD8 cleavage assays, the coding sequences of human CARD8 (NCBI accession

403   NP_001171829.1), human CARD8 mutants (Q37A, Q37A Q61A, S39P, R40W), human CARD8

404   TEV, *Rousettus aegyptiacus* (megabat) CARD8 (NCBI accession XP_016010896), and megabat

405   CARD8 TEV were cloned into the pcDNA5/FRT/TO backbone (Invitrogen, Carlsbad, CA) with

406   an N-terminal 3xFlag-mCherry tag. For CARD8 activation, the same sequences were cloned into

407   the pQCXIP vector backbone (Takara Bio, Mountain View, CA) with a C-terminal Myc tag.

408   Megabat CASP1 (NCBI accession KAF6464288) and megabat IL-1β (NCBI accession

409   KAF6447073), also from *Rousettus aegyptiacus*, were cloned in the same vector as their

410   respective human orthologues. 3CL^{pro} sequences were cloned with an N-terminal HA tag into the

21

411 QCXIP vector backbone, flanked by polyprotein cleavage sites fused to N-terminal eGFP and C-

412 terminal mCherry (**S2 Fig)**. 3C^{pro} constructs were described previously (*11*).

413   Single point mutations were made using overlapping stitch PCR. All plasmid stocks were

414 sequenced across the entire inserted region to verify that no mutations were introduced during

415 the cloning process. The primers used for cloning are described in **S7 Table**.

416

417 *Cell culture and transient transfection*

418 All cell lines (HEK293T, HEK-Blue-IL-1β) are routinely tested for mycoplasma by PCR kit

419 (ATCC, Manassas, VA) and kept a low passage number to maintain less than one year since

420 purchase, acquisition or generation. HEK293T cells were obtained from ATCC (catalog # CRL-

421 3216) and HEK-Blue-IL-1β cells were obtained from Invivogen (catalog # hkb-il1b) and all lines

422 were verified by those sources, and were grown in complete media containing DMEM (Gibco,

423 Carlsbad, CA), 10% FBS, and appropriate antibiotics (Gibco, Carlsbad, CA). THP-1 cells were

424 purchased from ATCC, and grown in complete media containing RPMI (Gibco, Carlsbad, CA)

425 10% FBS, and 1% L-glutamine. For transient transfections, HEK293T cells were seeded the day

426 prior to transfection in a 24-well plate (Genesee, El Cajon, CA) with 500 µl complete media.

427 Cells were transiently transfected with 500 ng of total DNA and 1.5 µl of Transit X2 (Mirus Bio,

428 Madison, WI) following the manufacturer's protocol. HEK-Blue IL-1β reporter cells (Invivogen,

429 San Diego, CA) were grown and assayed in 96-well plates (Genesee, El Cajon, CA).

430

431 *Generation of knockout and transgenic cell lines*

432 *CARD8* knockouts in HEK293T cells were generated similarly to *NLRP1* knockouts described in

433 (*11*). Briefly, lentivirus-like particles were made by transfecting HEK293T cells with the

22

434   plasmids psPAX2 (gift from Didier Trono, Addgene plasmid # 12260), pMD2.G (gift from

435   Didier Trono, Addgene plasmid # 12259), and either pLB-Cas9 (gift from Feng Zhang, Addgene

436   plasmid # 52962) (*56*) or plentiGuide-Puro, which was adapted for ligation-independent cloning

437   (gift from Moritz Gaidt) (*57*). Conditioned supernatant was harvested 48 and 72 hours post-

438   transfection and used for spinfection of HEK293T cells at 1200 x *g* for 90 minutes at 32°C.

439   Forty-eight hours post-spinfection, cells with stable expression of Cas9 were selected in media

440   containing 100 µg/ml blasticidin. Blasticidin-resistant cells were then transduced with sgRNA-

441   encoding lentivirus-like particles, and selected in media containing 0.5 µg/ml puromycin. Cells

442   resistant to blasticidin and puromycin were single cell cloned by limiting dilution in 96-well

443   plates, and confirmed as knockouts by Sanger sequencing. *CARD8* knockout THP-1 cells were

444   generated as described previously (*58*). Briefly, a CARD8 specific sgRNA was designed using

445   CHOPCHOP (*59*), and cloned into a plasmid containing U6-sgRNA-CMV-mCherry-T2A-Cas9

446   using ligation-independent cloning. THP-1 cells were electroporated using the BioRad

447   GenePulser Xcell. After 24 h, mCherry-positive cells were sorted and plated for cloning by

448   limiting dilution. Monoclonal lines were validated as knockouts by deep sequencing and

449   OutKnocker analysis, as described previously (*60, 61*). Knockout lines were further validated by

450   immunoblot and functional assays. sgRNA used to generate knockouts are described in **S7**

451   **Table**. To make THP-1 cells susceptible to SARS-CoV-2 infection(*62*), ACE2 and TMPRSS2

452   expressing THP-1 cells were made using the same lentiviral transduction protocol as described

453   above, but using the transfer plasmid PpWIP-IRES-Bla-AK-ACE2-IRES-TMPRSS2 (gift from

454   Sonja Best). THP-1 cells were selected with 10 µg/ml blasticidin.

455

456   *THP-1 treatments and viral infections*

23

457 50,000-100,000 THP-1 cells per well in 96-well round bottom plates in 50 µl OptiMEM

458 containing 500 ng/mL Pam3CSK4 for 6h, followed by treatment with Val-boroPro (10µM) or

459 infection with the coronaviruses hCoV-229E (BEI NR-52726) or SARS-CoV-2 (USA/WA-

460 1/2020, a gift from Dr. Ralph Baric) at indicated multiplicities of infection (MOIs). 48h post-

461 treatment or infection, supernatants were harvested for the detection of IL-1β (see below). Cells

462 were transferred to a white-walled 96-well assay plate and mixed with an equal volume of Cell

463 Titer Glo reagent (Promega). Measurements for fluorescence at 544-15 nm (excitation), 620-20

464 nm (emission) or luminescence at 555-70 (emission) were taken following incubation at room

465 temperature, rocking for 10min.

466

467 *CARD8 cleavage assays*

468 100 ng of epitope-tagged human CARD8 (WT, Q37A, Q37A Q61A, S39P, R40W), human

469 CARD8 TEV, megabat CARD8 WT or megabat CARD8 TEV was co-transfected with either

470 HA-tagged QCXIP empty vector ('-'), 250 ng of TEV^{pro}, 250 ng of untagged HIV-1^{pro} (HIV-1

471 gag-pol carrying HIV-1 protease activity), 5 ng of HA-tagged 3CL^{pro}, or 250 ng of HA-tagged

472 3C^{pro}-encoding constructs. Twenty-four hours post-transfection, the cells were harvested, lysed

473 in 1x NuPAGE LDS sample buffer (Invitrogen, Carlsbad, CA) containing 5% β-mercaptoethanol

474 (Fisher Scientific, Pittsburg, PA) and immunoblotted with antibodies described in **S8 Table**.

475

476 *CARD8 activity assays*

477 To reconstitute the human CARD8 inflammasome, 100 ng of human CASP1 and 50 ng of human

478 IL-1β-V5 were co-transfected with 50 ng of either HA-tagged QCXIP empty vector, wild-type or

479 mutant pQCXIP-CARD8-Myc constructs in *CARD8* KO HEK293T cells. To reconstitute the

24

480 megabat CARD8 inflammasome, 10 ng of megabat CASP1 and 50 ng of megabat IL-1β-V5

481 were co-transfected with 2 ng megabat CARD8 constructs in *CARD8* KO HEK293T cells. These

482 cells were further co-transfected with either empty vector ('-'), 250 ng of TEV^pro, 100 ng of

483 untagged HIV-1 gag-pol (with HIV-1 protease activity), 5 ng of HA-tagged 3CL^pro, 100 ng of

484 HA-tagged enteroviral 3C^pro, or 20 ng of HA-tagged non-enteroviral 3C^pro-encoding constructs.

485 Twenty-four hours post-transfection, cells were harvested and lysed in 1x NuPAGE LDS sample

486 buffer containing 5% β-mercaptoethanol and immunoblotted with antibodies described in **S8**

487 **Table** or culture media was harvested for quantification of IL-1β levels by HEK-Blue assays (see

488 below). Appearance of the mature p17 band of IL-1β indicates successful assembly and

489 activation of the inflammasome.

490

491 *HEK-Blue IL-1β assay*

492 To quantify the levels of bioactive IL-1β released from cells, we employed HEK-Blue IL-1β

493 reporter cells (Invivogen, San Diego, CA). In these cells, binding to IL-1β to the surface receptor

494 IL-1R1 results in the downstream activation of NF-kB and subsequent production of secreted

495 embryonic alkaline phosphatase (SEAP) in a dose-dependent manner (*11*). SEAP levels are

496 detected using a colorimetric substrate assay, QUANTI-Blue (Invivogen, San Diego, CA) by

497 measuring an increase in absorbance at OD655.

498   Culture supernatant from inflammasome-reconstituted HEK293T cells or HEK293T

499 *CARD8* KO cells that had been transfected with 3CL pro was added to HEK-Blue IL-1β reporter

500 cells plated in 96-well format in a total volume of 200 μl per well. On the same plate, serial

501 dilutions of recombinant human IL-1β (Invivogen, San Diego, CA) were added to generate a

502 standard curve for each assay. Twenty-four hours later, SEAP levels were assayed by taking 20

503   µl of the supernatant from HEK-Blue IL-1β reporter cells and adding to 180 µl of QUANTI-Blue

504   colorimetric substrate following the manufacturer's protocol. After incubation at 37°C for 30–60

505   min, absorbance at OD655 was measured on a BioTek Cytation five plate reader (BioTek

506   Instruments, Winooski, VT) and absolute levels of IL-1β were calculated relative to the standard

507   curve. All assays, beginning with independent transfections or infections, were performed in

508   triplicate.

509

510   *Immunoblotting and antibodies*

511   Harvested cell pellets were washed with 1X PBS, and lysed with 1x NuPAGE LDS sample

512   buffer containing 5% β-mercaptoethanol at 98C for 10 min. The lysed samples were spun down

513   at 15000 RPM for two minutes, followed by loading into a 4–12% Bis-Tris SDS-PAGE gel (Life

514   Technologies, San Diego, CA) with 1X MOPS buffer (Life Technologies, San Diego, CA) and

515   wet transfer onto a nitrocellulose membrane (Life Technologies, San Diego, CA). Membranes

516   were blocked with PBS-T containing 5% bovine serum albumin (BSA) (Spectrum, New

517   Brunswick, NJ), followed by incubation with primary antibodies for V5 (IL-1β), FLAG

518   (mCherry-fused CARD8 for protease assays), Myc (CARD8-Myc for activation assays), HA

519   (viral protease), or GAPDH. Membranes were rinsed three times in PBS-T then incubated with

520   the appropriate HRP-conjugated secondary antibodies. Membranes were rinsed again three times

521   in PBS-T and developed with SuperSignal West Pico PLUS Chemiluminescent Substrate

522   (Thermo Fisher Scientific, Carlsbad, CA). The specifications, source, and clone info for

523   antibodies are described in **S8 Table**.

524

525

26

531   **References**

532   1.   J. D. Jones, R. E. Vance, J. L. Dangl, Intracellular innate immune surveillance devices in

533   plants and animals. Science 354, (2016).

534   2.   R. E. Vance, R. R. Isberg, D. A. Portnoy, Patterns of pathogenesis: discrimination of

535   pathogenic and nonpathogenic microbes by the innate immune system. Cell Host

536   Microbe 6, 10-21 (2009).

537   3.   P. S. Mitchell, A. Sandstrom, R. E. Vance, The NLRP1 inflammasome: new mechanistic

538   insights and unresolved mysteries. Curr Opin Immunol 60, 37-45 (2019).

539   4.   H. Cui, K. Tsuda, J. E. Parker, Effector-triggered immunity: from pathogen perception to

540   robust defense. Annu Rev Plant Biol 66, 487-511 (2015).

541   5.   N. L. Fischer, N. Naseer, S. Shin, I. E. Brodsky, Publisher Correction: Effector-triggered

542   immunity and pathogen sensing in metazoans. Nat Microbiol 5, 528 (2020).

543   6.   P. Broz, V. M. Dixit, Inflammasomes: mechanism of assembly, regulation and signalling.

544   Nat Rev Immunol 16, 407-420 (2016).

545   7.   C. L. Evavold, J. C. Kagan, Inflammasomes: Threat-Assessment Organelles of the Innate

546   Immune System. Immunity 51, 609-624 (2019).

547   8.   V. A. Rathinam, K. A. Fitzgerald, Inflammasome Complexes: Emerging Mechanisms

548   and Effector Functions. Cell 165, 792-800 (2016).

549   9.   R. Planes et al., Human NLRP1 is a sensor of pathogenic coronavirus 3CL proteases in

550   lung epithelial cells. Mol Cell 82, 2385-2400 e2389 (2022).

551   10.   K. S. Robinson et al., Enteroviral 3C protease activates the human NLRP1 inflammasome

552   in airway epithelia. Science 370, (2020).

553   11.   B. V. Tsu et al., Diverse viral proteases activate the NLRP1 inflammasome. Elife 10,

554   (2021).

555   12.   Q. Wang et al., CARD8 is an inflammasome sensor for HIV-1 protease activity. Science

556   371, (2021).

557   13.   A. J. Chui et al., N-terminal degradation activates the NLRP1B inflammasome. Science

558   364, 82-85 (2019).

559   14.   A. Sandstrom et al., Functional degradation: A mechanism of NLRP1 inflammasome

560   activation by diverse pathogen enzymes. Science 364, (2019).

561   15.   B. V. Tsu et al., Running With Scissors: Evolutionary Conflicts Between Viral Proteases

562   and the Host Immune System. Front Immunol 12, 769543 (2021).

563   16.   S. Chen et al., Feline Infectious Peritonitis Virus Nsp5 Inhibits Type I Interferon

564   Production by Cleaving NEMO at Multiple Sites. Viruses 12, (2019).

565   17.   M. Moustaqil et al., SARS-CoV-2 proteases PLpro and 3CLpro cleave IRF3 and critical

566   modulators of inflammatory pathways (NLRP12 and TAB1): implications for disease

567   presentation across species. Emerg Microbes Infect 10, 178-195 (2021).

568   18.   X. Zhu et al., Porcine deltacoronavirus nsp5 inhibits interferon-beta production through

569   the cleavage of NEMO. Virology 502, 33-38 (2017).

570   19.   X. Zhu et al., Porcine Deltacoronavirus nsp5 Antagonizes Type I Interferon Signaling by

571   Cleaving STAT2. J Virol 91, (2017).

572   20.   C. P. Chuck et al., Profiling of substrate specificity of SARS-CoV 3CL. PLoS One 5,

573   e13197 (2010).

574   21.   C. P. Chuck, H. F. Chow, D. C. Wan, K. B. Wong, Profiling of substrate specificities of

575   3C-like proteases from group 1, 2a, 2b, and 3 coronaviruses. PLoS One 6, e27228 (2011).

576   22.   S. Fang, H. Shen, J. Wang, F. P. Tay, D. X. Liu, Functional and genetic studies of the

577   substrate specificity of coronavirus infectious bronchitis virus 3C-like proteinase. J Virol

578   84, 7325-7336 (2010).

579   23.   D. H. Goetz et al., Substrate specificity profiling and identification of a new class of

580   inhibitor for the major protease of the SARS coronavirus. Biochemistry 46, 8744-8752

581   (2007).

582   24.   J. Chavarria-Smith, P. S. Mitchell, A. M. Ho, M. D. Daugherty, R. E. Vance, Functional

583   and Evolutionary Analyses Identify Proteolysis as a General Mechanism for NLRP1

584   Inflammasome Activation. PLoS Pathog 12, e1006052 (2016).

585   25.   A. D'Osualdo et al., CARD8 and NLRP1 undergo autoproteolytic processing through a

586   ZU5-like domain. PLoS One 6, e27396 (2011).

587   26.   D. C. Johnson et al., DPP8/9 inhibitors activate the CARD8 inflammasome in resting

588   lymphocytes. Cell Death Dis 11, 628 (2020).

589   27.   M. K. Roe, N. A. Junod, A. R. Young, D. C. Beachboard, C. C. Stobart, Targeting novel

590   structural and functional features of coronavirus protease nsp5 (3CL(pro), M(pro)) in the

591   age of COVID-19. J Gen Virol 102, (2021).

592   28.   A. Linder et al., CARD8 inflammasome activation triggers pyroptosis in human T cells.

593   EMBO J 39, e105071 (2020).

594   29.   T. S. Rodrigues et al., Inflammasomes are activated in response to SARS-CoV-2

595   infection and are associated with COVID-19 severity in patients. J Exp Med 218, (2021).

596   30.   E. Sefik et al., Inflammasome activation in infected macrophages drives COVID-19

597   pathology. Nature 606, 585-593 (2022).

598   31.   C. Junqueira et al., FcgammaR-mediated SARS-CoV-2 infection of monocytes activates

599   inflammation. Nature 606, 576-584 (2022).

600   32.   M. D. Daugherty, H. S. Malik, Rules of engagement: molecular insights from host-virus

601   arms races. Annu Rev Genet 46, 677-700 (2012).

602   33.   M. Sironi, R. Cagliani, D. Forni, M. Clerici, Evolutionary insights into host-pathogen

603   interactions from mammalian sequence data. Nat Rev Genet 16, 224-236 (2015).

604   34.   S. Rothenburg, G. Brennan, Species-Specific Host-Virus Interactions: Implications for

605   Viral Host Range and Virulence. Trends Microbiol 28, 46-56 (2020).

606   35.   M. Letko, S. N. Seifert, K. J. Olival, R. K. Plowright, V. J. Munster, Bat-borne virus

607   diversity, spillover and emergence. Nat Rev Microbiol 18, 461-471 (2020).

608   36.   V. D. Menachery et al., A SARS-like cluster of circulating bat coronaviruses shows

609   potential for human emergence. Nat Med 21, 1508-1513 (2015).

610   37.   R. R. da Fonseca, C. Kosiol, T. Vinar, A. Siepel, R. Nielsen, Positive selection on

611   apoptosis related genes. FEBS Lett 584, 469-476 (2010).

612   38.   K. J. Karczewski et al., The mutational constraint spectrum quantified from variation in

613   141,456 humans. Nature 581, 434-443 (2020).

614   39.   L. Bouchier-Hayes et al., CARDINAL, a novel caspase recruitment domain protein, is an

615   inhibitor of multiple NF-kappa B activation pathways. J Biol Chem 276, 44069-44077

616   (2001).

617   40.   M. Yamamoto et al., A novel isoform of TUCAN is overexpressed in human cancer

618   tissues and suppresses both caspase-8- and caspase-9-mediated apoptosis. Cancer Res 65,

619   8706-8714 (2005).

620   41.   D. C. Johnson et al., DPP8/DPP9 inhibitor-induced pyroptosis for treatment of acute

621   myeloid leukemia. Nat Med 24, 1151-1156 (2018).

622   42.   R. D. Bagnall et al., Novel isoforms of the CARD8 (TUCAN) gene evade a nonsense

623   mutation. Eur J Hum Genet 16, 619-625 (2008).

624   43.   K. P. Y. Hui et al., Tropism, replication competence, and innate immune responses of the

625   coronavirus SARS-CoV-2 in human respiratory tract and conjunctiva: an analysis in ex-

626   vivo and in-vitro cultures. Lancet Respir Med 8, 687-695 (2020).

627   44.   S. M. Vora, J. Lieberman, H. Wu, Inflammasome activation at the crux of severe

628   COVID-19. Nat Rev Immunol 21, 694-703 (2021).

629   45.   J. K. Y. Yap, M. Moriyama, A. Iwasaki, Inflammasomes and Pyroptosis as Therapeutic

630   Targets for COVID-19. J Immunol 205, 307-312 (2020).

631   46.   D. P. Ball et al., Caspase-1 interdomain linker cleavage is required for pyroptosis. Life

632   Sci Alliance 3, (2020).

633   47.   B. E. Pickett et al., Virus pathogen database and analysis resource (ViPR): a

634   comprehensive bioinformatics database and analysis resource for the coronavirus

635   research community. Viruses 4, 3209-3226 (2012).

636   48.   K. Katoh, D. M. Standley, MAFFT multiple sequence alignment software version 7:

637   improvements in performance and usability. Mol Biol Evol 30, 772-780 (2013).

638   49.   M. Kearse et al., Geneious Basic: an integrated and extendable desktop software platform

639   for the organization and analysis of sequence data. Bioinformatics 28, 1647-1649 (2012).

640   50.   C. Camacho et al., BLAST+: architecture and applications. BMC Bioinformatics 10, 421

641   (2009).

642   51.   Z. Yang, PAML 4: phylogenetic analysis by maximum likelihood. Mol Biol Evol 24,

643   1586-1591 (2007).

644   52.   B. Murrell et al., Gene-wide identification of episodic selection. Mol Biol Evol 32, 1365-

645   1371 (2015).

646   53.   S. Weaver et al., Datamonkey 2.0: A Modern Web Application for Characterizing

647   Selective and Other Evolutionary Processes. Mol Biol Evol 35, 773-777 (2018).

648   54.   S. L. Kosakovsky Pond, S. D. Frost, Not so different after all: a comparison of methods

649   for detecting amino acid sites under selection. Mol Biol Evol 22, 1208-1222 (2005).

650   55.   B. Murrell et al., FUBAR: a fast, unconstrained bayesian approximation for inferring

651   selection. Mol Biol Evol 30, 1196-1205 (2013).

652   56.   N. E. Sanjana, O. Shalem, F. Zhang, Improved vectors and genome-wide libraries for

653   CRISPR screening. Nat Methods 11, 783-784 (2014).

654   57.   T. Schmidt, J. L. Schmid-Burgk, V. Hornung, Synthesis of an arrayed sgRNA library

655   targeting the human genome. Sci Rep 5, 14987 (2015).

656   58.   M. M. Gaidt et al., Self-guarding of MORC3 enables virulence factor-triggered

657   immunity. Nature 600, 138-142 (2021).

658   59.   K. Labun et al., CHOPCHOP v3: expanding the CRISPR web toolbox beyond genome

659   editing. Nucleic Acids Res 47, W171-W174 (2019).

660   60.   J. L. Schmid-Burgk et al., OutKnocker: a web tool for rapid and simple genotyping of

661   designer nuclease edited cell lines. Genome Res 24, 1719-1723 (2014).

662   61.   T. Schmidt, J. L. Schmid-Burgk, T. S. Ebert, M. M. Gaidt, V. Hornung, Designer

663   Nuclease-Mediated Generation of Knockout THP1 Cells. Methods Mol Biol 1338, 261-

664   272 (2016).

665   62.   M. Hoffmann et al., SARS-CoV-2 Cell Entry Depends on ACE2 and TMPRSS2 and Is

666   Blocked by a Clinically Proven Protease Inhibitor. Cell 181, 271-280 e278 (2020).

667

Competing interests

669   Authors declare that they have no competing interests.

670

Author contributions:

687   Conceptualization: BVT, PSM, MDD
688   Methodology: BVT, NSG, JK, APR, EAT, PSM, MDD
689   Investigation: BVT, RA, NSG, JK, APR, LKC, CMB, EAT, EJF, PSM, MDD
690   Visualization: BVT, NSG, PSM, MDD
691   Funding acquisition: REV, PSM, MDD
692   Project administration: REV, JLH, RS, PSM, MDD
693   Supervision: REV, JLH, RS, PSM, MDD
694   Writing – original draft: BVT, PSM, MDD
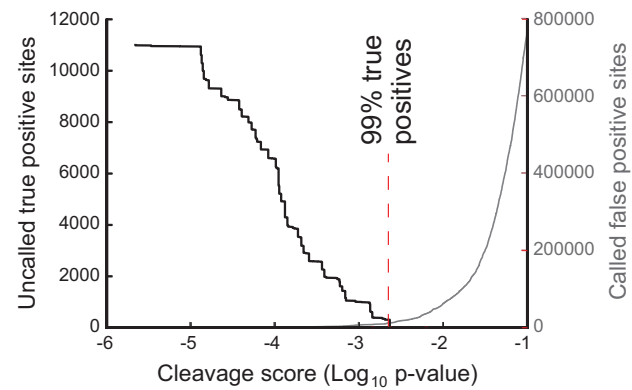695   Writing – review & editing: All authors

696   **Supporting Information**
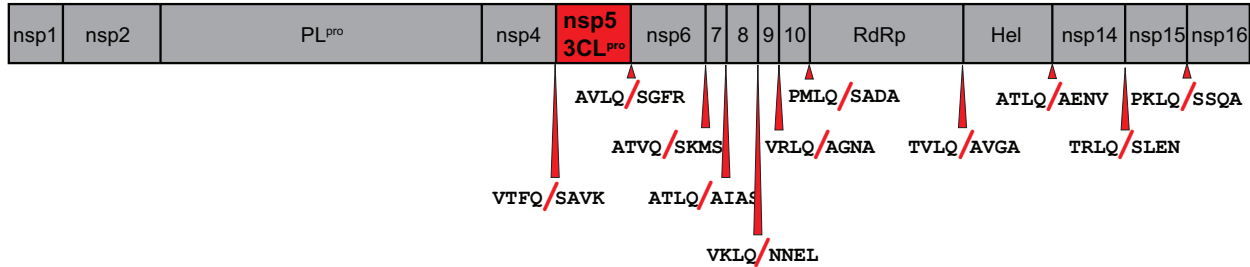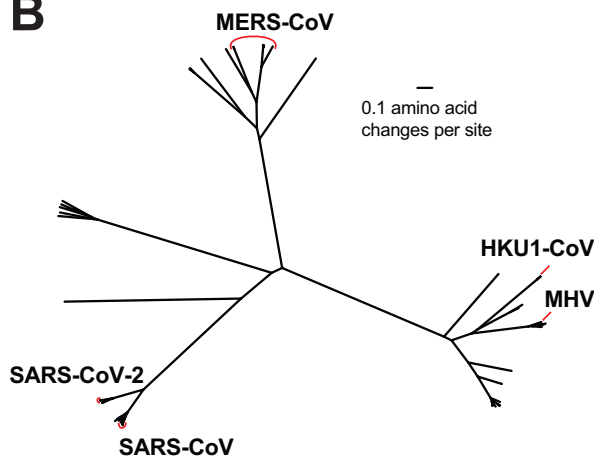
697
698   **S1 Fig. Motif generation of coronaviral 3CL^{pro} polyprotein cleavage.**

699   (A) Schematic of 3CL^{pro} cleavage sites (11 red triangles) within the polyprotein of SARS-CoV-2
700   (SARS-2), the causative agent of COVID-19. Shown are four amino acids flanking each side of
701   the cleavage site within the polyprotein. (B) Phylogenetic tree of 60 coronavirus polyprotein
702   coding sequences depicting the betacoronaviruses sampled in this study with human relevant
703   coronaviruses labeled (table S2). (C) Training set data used to determine the motif search
704   threshold for FIMO (table S1). The X-axis represents a log10 of the p-value reported by FIMO
705   as an indicator for the strength of the cleavage motif hit (cleavage score). (Left) The Y-axis
706   depicts the number of uncalled true positives, or motif hits that overlap with the initial set of
707   8mer polyprotein cleavage sites used to generate the motif, in the training set of coronavirus
708   polyprotein sequences (black line). (Right) The Y-axis depicts the number of called false positive
709   sites, or any motif hits found in the polyprotein that are not known to be cleaved by 3CL^{pro}, in
710   the training set of coronaviral polyprotein sequences (gray). A red vertical dashed line indicates
711   the threshold that captures 99% of true positive polyprotein hits (p-value = 0.00231).

34

A
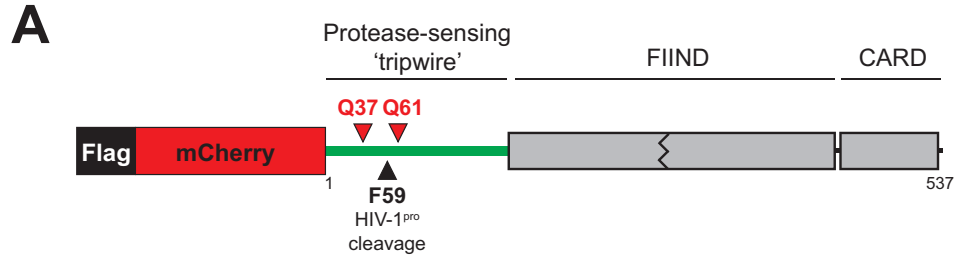
Predicted protein products

Full length CARD8 (92 kDa)

FIIND processed CARD8 (63 kDa)

3CL^{pro} cleaved CARD8 at site Q37 (34 kDa)

HIV-1^{pro} cleaved CARD8 at site F59 (37 kDa)

3CL^{pro} cleaved CARD8 at site Q61 (37 kDa)

B

Uncleaved 3CL^{pro} fusion protein (92 kDa)

3CL^{pro} cleavage product (30 kDa)

C

712

35
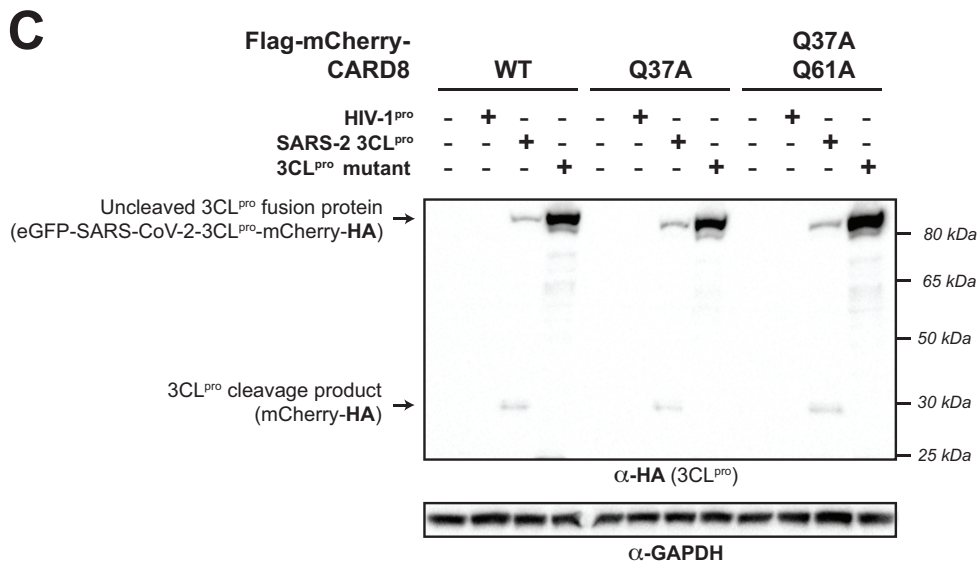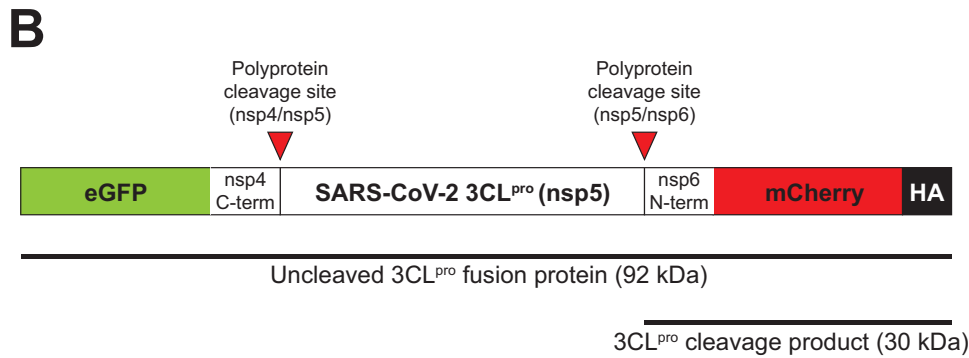
713 **S2 Fig. Schematic of CARD8 and 3CL^{pro} expression constructs for cleavage assays and**
714 **immunoblot depicting HA-tagged SARS-2 3CL^{pro} and SARS-2 3CL^{pro} mutant.**
715 (A) Schematic of the expression constructs used for CARD8 cleavage assays. Full length
716 CARD8 was fused to a 3xFlag-mCherry domain to increase the stability and our ability to detect
717 viral protease cleavage products in the N-terminus of CARD8. Below are shown the expected
718 sizes of full length and FIIND processed CARD8, as well as the expected sizes that would result
719 from viral protease cleavage at the indicated sites. (B) Schematic of the expression constructs
720 used for 3CL^{pros} (nsp5s). A region of the viral polyprotein spanning the C-terminal nine residues
721 of nsp4 through the N-terminal nine residues of nsp6 was cloned between eGFP and mCherry-
722 HA. Inactive protease is expressed as a full-length fusion protein (92 kDa predicted molecular
723 weight). Active 3CL^{pro} cleaves at the indicated polyprotein cleavage sites (red triangles),
724 liberating the active protease from the construct and resulting in an HA-tagged mCherry product
725 (30 kDa predicted molecular weight). (C) An expanded view of the anti-HA-stained immunoblot
726 shown in Figure 1B highlighting uncleaved (Uncleaved 3CL^{pro} fusion protein) and cleaved
727 (3CL^{pro} cleavage product) HA-tagged protein products.

36

728
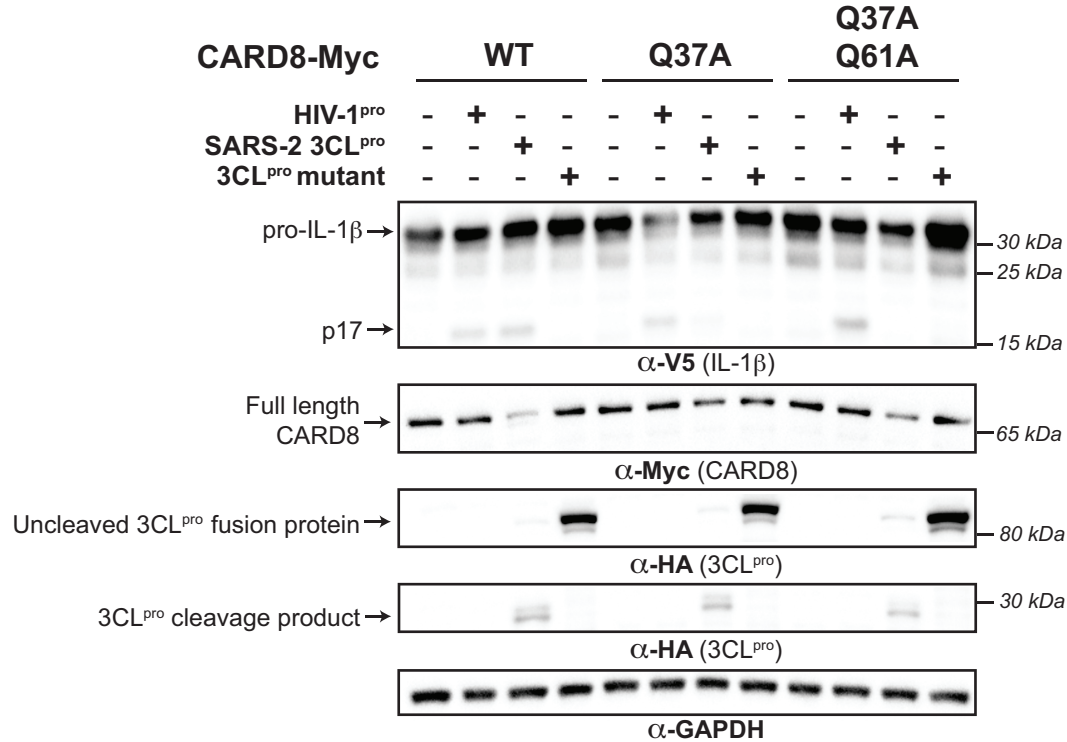
S3 Fig. CARD8 cleavage by viral proteases results in inflammasome activation and IL-1β maturation.

CARD8 inflammasome assay. CARD8 KO HEK293T cells were co-transfected using the indicated Myc-tagged CARD8 plasmid constructs, V5-IL-1β, CASP1, and HA-tagged protease constructs (SARS-CoV-2 3CL^{pro} (SARS-2 3CL^{pro}), SARS-CoV-2 3CL^{pro} catalytic mutant C145A (3CL^{pro} mutant), HIV-1 gag-pol (HIV-1^{pro}), or empty vector (-)). Appearance of a mature bioactive IL-1β (p17) indicates inflammasome activation.

736
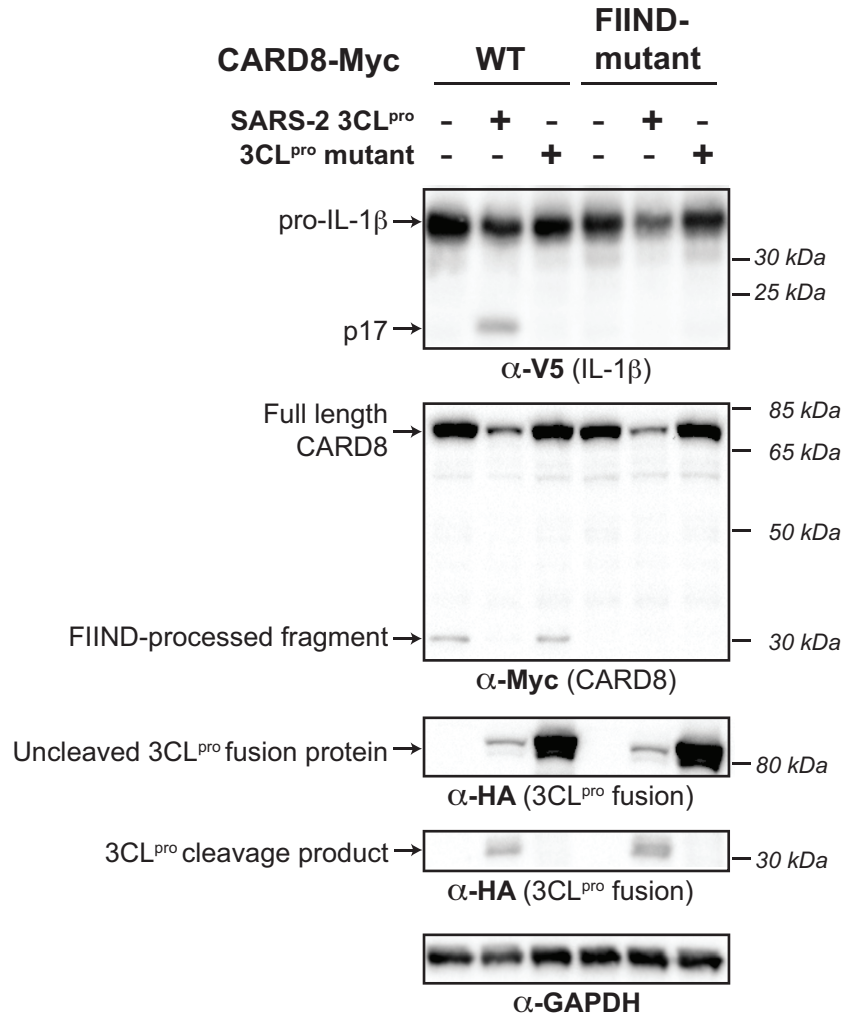
S4 Fig. 3CL^pro-mediated activation of the human CARD8 inflammasome depends on FIIND autoprocessing.

CARD8 inflammasome activation assay depicting loss of CARD8 activation with a FIIND autoprocessing mutant (S297A).

741
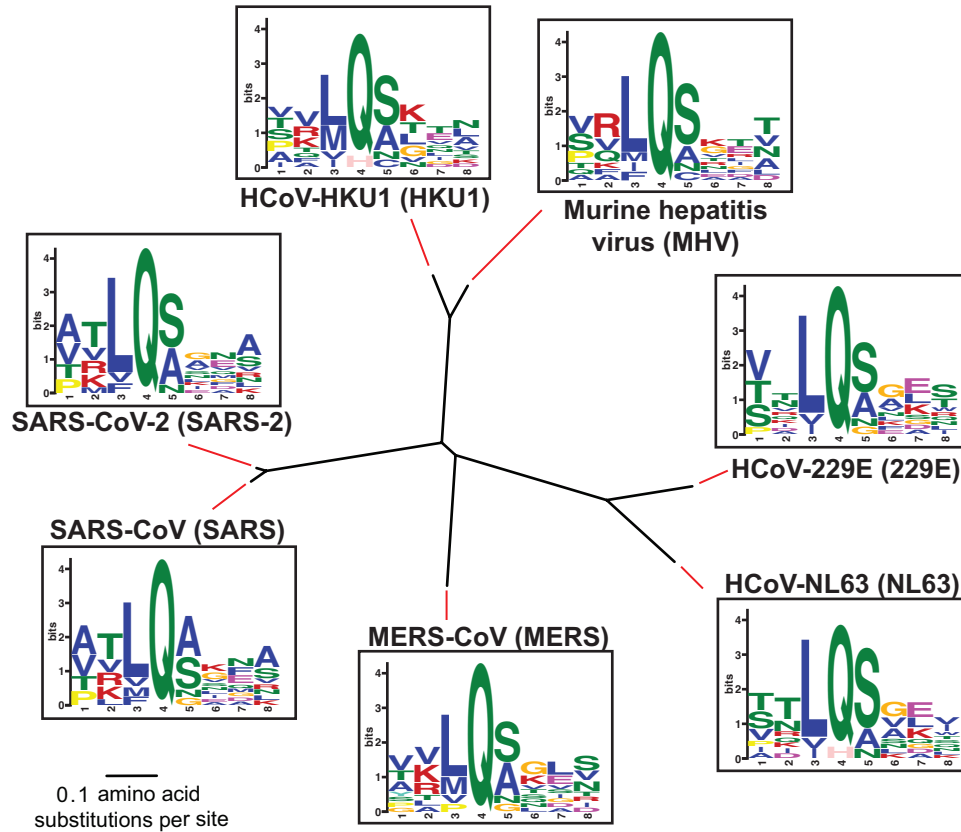
S5 Fig. 3CL^{pros} used in this study demonstrate similar polyprotein cleavage.
Phylogenetic tree of 3CL^{pro} protein sequences used in this study from the indicated coronaviruses. Shown next to the virus name is the sequence motif generated from the 3CL^{pro} polyprotein cleavage sites from that specific virus.
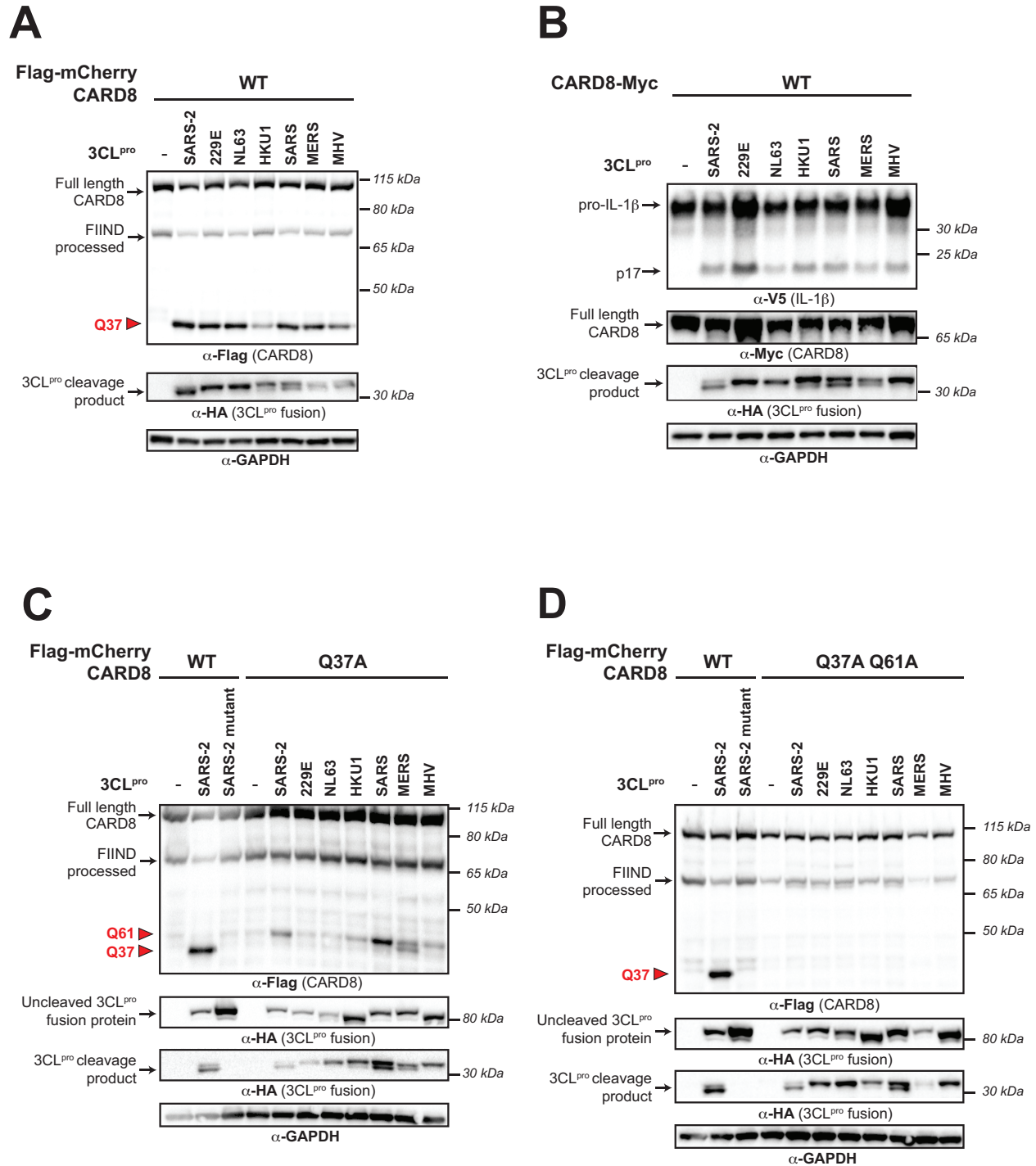
S6 Fig. Site-specific CARD8 cleavage and inflammasome activation by diverse coronavirus 3CL^{pros}.

(A) Cleavage assay depicting cleavage of human CARD8 by the indicated 3CL^{pros} from diverse coronaviruses (SARS-CoV-2 (SARS-2), HCoV-229E (229E), HCoV-NL63 (NL63), HCoV-HKU1 (HKU1), SARS-CoV (SARS), MERS-CoV (MERS), and murine hepatitis virus (MHV)). (B) CARD8 inflammasome activation assay with human CARD8 WT and the indicated 3CL^{pro}.

753   (C-D) Cleavage assays mapping the cleavage specificity of diverse 3CL^{pros}. Indicated proteases
754   were co-transfected with WT and Q37A (C) or Q37A Q61A (D).
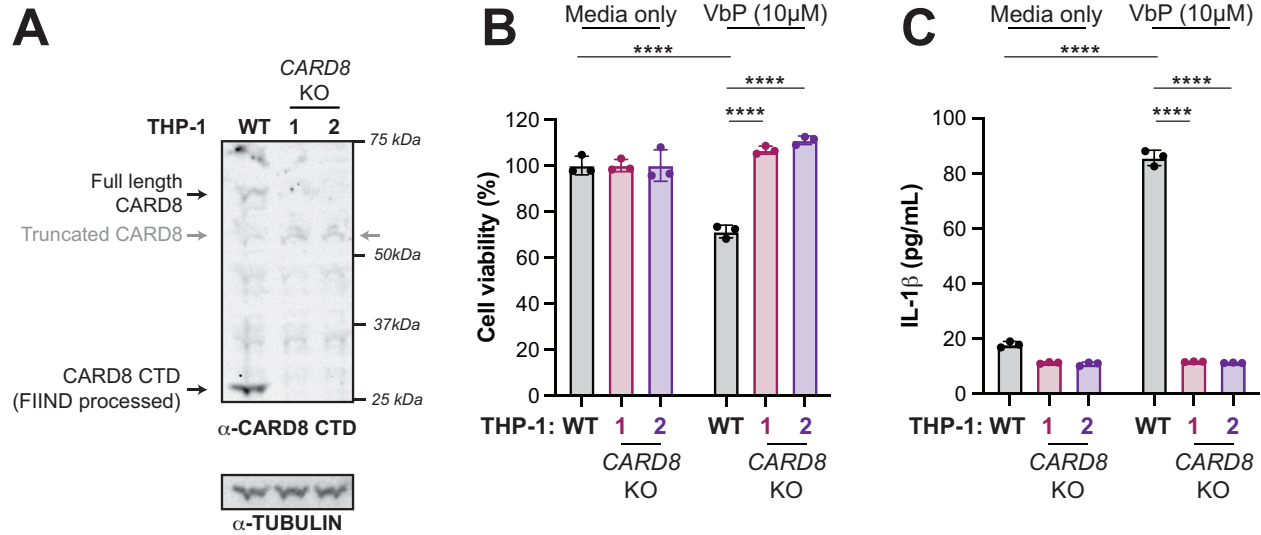
S7 Fig. Validation of *CARD8* KO THP-1 cells.

(A) Immunoblot of wildtype (WT) or *CARD8* knockout (KO) 1 and KO2 THP-1 cells. The sgRNA used to edit *CARD8* results in a truncated CARD8 (grey arrow) that removes the C-terminal domain (CTD), including the CARD. (B-C) Indicated THP-1 cells were primed with 0.5 µg/mL Pam3CSK4 for 6h, followed by treatment with 10 µM Val-boroPro (VbP) or media only. Cell viability (B) was measured 48h post-treatment via the Cell Titer Glo assay and IL-1β levels (C) were measured from cell supernatants using the IL1R reporter assay as in **Fig 1D** (see **Methods**). Data presented are representative of experiments performed in triplicate. Data were analyzed using two-way ANOVA with Šidák's post-test: p<0.0001.

Q349

Species	Sequence
Rousettus aegyptiacus (XP_016010887.2)	VRLQSSPP
Mammalian consensus sequence	VRLQTSPP
Dasypus novemcinctus (XP_004455135.1)	KRLQTSPP
Choloepus didactylus (XP_037676345.1)	VRLQTSPP
Orycteropus afer afer (XP_007941216.2)	VRLQTSPP
Echinops telfairi (XP_045148583.1)	VRLQTSPP
Elephas maximus indicus (XP_049756664.1)	VRLQNSPP
Trichechus manatus latirostris (XP_023591965.1)	VRLQTSPP
Loxodonta africana (XP_023398968.1)	VRLQTSPP
Tupaia chinensis (XP_006142263.2)	VRLQTSPP
Otolemur garnettii (XP_023363700.1)	VRLQTSPP
Carlito syrichta (XP_008065260.1)	VRLQTSPP
Callithrix jacchus (XP_008986567.2)	VRLQTSPP
Aotus nancymaae (XP_021524182.1)	VRLQTSPP
Saimiri boliviensis boliviensis (XP_003940505.2)	VRLQTSPP
Cebus imitator (XP_017355929.1)	VRLQTSPP
Sapajus apella (XP_032126901.1)	VRLQTSPP
Pongo abelii (NP_001125643.1)	VRLQTSPP
Nomascus leucogenys (XP_030676824.1)	VRLQTSPP
Hylobates moloch (XP_032025189.1)	VRLQTSPP
Homo sapiens (NP_001171829.1)	VRLQTSPP
Gorilla gorilla gorilla (XP_030860007.1)	VRLQTSPP
Pan paniscus (XP_034801359.1)	VRLQTSPP
Pan troglodytes (XP_009434234.2)	VRLQTSPP
Rhinopithecus bieti (XP_017744314.1)	VRLQTSPP
Rhinopithecus roxellana (XP_030798493.1)	VRLQTSPP
Macaca mulatta (XP_028694412.1)	VRLQTSPP
Cercocebus atys (XP_011936103.1)	VRLQTSPP
Papio anubis (XP_031516220.1)	VRLQTSXP
Theropithecus gelada (XP_025223748.1)	VRLQTSPP
Papio anubis (XP_031514956.1)	VRLQTSPS
Macaca fascicularis (XP_045236836.1)	VRLQTSPS
Macaca nemestrina (XP_011734426.1)	VRLQTSPS
Chlorocebus sabaeus (XP_037847268.1)	VRLQTSPS
Mandrillus leucophaeus (XP_011831805.1)	VRLQTSPS
Colobus angolensis palliatus (XP_011801863.1)	VRLQTSPS
Trachypithecus francoisi (XP_033079741.1)	VRLQTSPP
Ceratotherium simum simum (XP_014650570.1)	VRLQTSPP
Rousettus aegyptiacus (XP_016010887.2)	VRLQSSPP
Pteropus alecto (XP_006905198.1)	VRLQSSAP
Pteropus vampyrus (XP_011376482.1)	VRLQSSAP
Pteropus giganteus (XP_039724536.1)	VRLQSSAP
Hyaena hyaena (XP_039104475.1)	VRLQTSPP
Puma concolor (XP_025770087.1)	VRLQTSPP
Leopardus geoffroyi (XP_045296688.1)	VRLQTSPP
Felis catus (XP_006941207.3)	VRLQTSPP
Prionailurus bengalensis (XP_043456356.1)	VRLQTSPP
Prionailurus viverrinus (XP_047693116.1)	VRLQTSPP
Lynx canadensis (XP_030155679.1)	VRLQTSPP
Lynx rufus (XP_046933669.1)	VRLQTSPP
Puma yagouaroundi (XP_040313498.1)	VRLQTSPP
Acinonyx jubatus (XP_014938520.1)	VRLQTSPP
Panthera tigris (XP_007074174.1)	VRLQTSPP
Panthera uncia (XP_049478262.1)	VRLQTSPP
Panthera leo (XP_042775368.1)	VRLQTSPP
Panthera pardus (XP_019281377.1)	VRLQTSPP
Vulpes vulpes (XP_025869883.1)	VRLQTSPP
Canis lupus familiaris (XP_038316790.1)	VRLQTSPP
Canis lupus dingo (XP_025280236.1)	VRLQTSPP
Odobenus rosmarus divergens (XP_004401075.2)	VRLQTSPP
Callorhinus ursinus (XP_025705476.1)	VRLQTSPP
Zalophus californianus (XP_027475647.1)	VRLQTSPP
Eumetopias jubatus (XP_027943719.1)	VRLQTSPP
Halichoerus grypus (XP_035955734.1)	VRLQTSPP
Phoca vitulina (XP_032244836.1)	VRLQTSPP
Leptonychotes weddellii (XP_030897212.1)	VRLQTSPP
Neomonachus schauinslandi (XP_021536893.1)	VRLQTSPP
Mirounga angustirostris (XP_045746402.1)	VRLQTSPP
Mirounga leonina (XP_034842787.1)	VRLQTSPP
Ailuropoda melanoleuca (XP_002917973.3)	VRLQTSPP
Ursus arctos (XP_026337717.1)	VRLQTSPP
Ursus maritimus (XP_008682721.1)	VRLQTSPP
Ursus americanus (XP_045628234.1)	VRLQTSPP
Meles meles (XP_045843773.1)	IRLQTSPP
Neogale vison (XP_044116462.1)	VRLQTSPP
Mustela erminea (XP_032179857.1)	VRLQTSPP
Mustela putorius furo (XP_004767506.1)	VRLQTSPP
Lontra canadensis (XP_032694832.1)	VRLQTSPP
Lutra lutra (XP_047567415.1)	VRLQTSPP
Enhydra lutris kenyoni (XP_022379885.1)	VRLQTSPP

Megabats

765

43

766 **S8 Fig. A coronavirus 3CL^pro cleavage site in the CARD8 C-terminus is unique to**
767 **megabats.**
768 An alignment of protein sequences homologous to the coronavirus 3CL^pro cleavage site in
769 megabat (*Rousettus aegyptiacus*) CARD8 is shown for indicated species (scientific name,
770 accession number). Amino acid numbering is based on *R. aegyptiacus* CARD8. Changes relative
771 to the consensus, depicted as a sequence logo at the top of the alignment) are highlighted. Four
772 species of megabats are indicated, and are unique in having a serine in the P1' position of the
773 cleavage site (highlighted in red). Most other species have a threonine in this position, which
774 makes the protein uncleavable at this site (**Fig 3E).**

```
                                                   Q37                        F59 Q61
                                                    ▼                          ▼  ▼
        Human reference           EELPRRDSGSSRNIDASKLIRLQGSRKLLVDNSIRELQYTKTGIFFQAEAC
                                  15                                                65
 Human SNP rs12463023 (P39)       EELPRRDSGSSRNIDASKLIRLQGPRKLLVDNSIRELQYTKTGIFFQAEAC
Human SNP rs138177358 (W40)       EELPRRDSGSSRNIDASKLIRLQGSWKLLVDNSIRELQYTKTGIFFQAEAC

                 Chimpanzee       EELPRPHSGSSRNTDASKLIRLQGPRKLLVDNSIRELQYTKTGIFLQAEAC
                     Bonobo       EELPRQHSGSSRNTDASKLIRLQGPRKLLVDNSIRELQYTKTGIFLQAEAC
        White-cheeked gibbon      EELPRPDRGSSRNVDASKLIRIQGPWNVLVDNSIRELQYTKTGIFSQAEAC
               Silvery gibbon     EELPRPDRGSSRNVDASKLIRIQGPWNVLVDNSIRELQYTKTGVFSQAEAC
             Rhesus macaque       EELWRRDNGSSRSVDASELVRQQ---TVLVDNSIQKLRDTRTGIFSQAEAC
          Crab-eating macaque     EELWRRDNGSSRSVDASELVRQQ---TVLVDNSIQKLRDTRTGIFSQAEAC
             Francois' langur     EELPRRNRGSSISVDASEVIRQQ---TVLVDDSIQKRRDTTTGIFSQAEAC
           Snub-nosed monkey      EELPRLHHGSSRNVDASEVIRQQ---TVLVDDSIQKRRDMTTGIFSQAEAC
```

775

S9 Fig. Rapid evolution and human polymorphism in the 'tripwire' region of CARD8 that is targeted by viral proteases.

An alignment of the CARD8 N-terminus (amino acids 15-65, where amino acid numbering is based on human CARD8) or 'tripwire' region from humans and selected non-human primates. Hum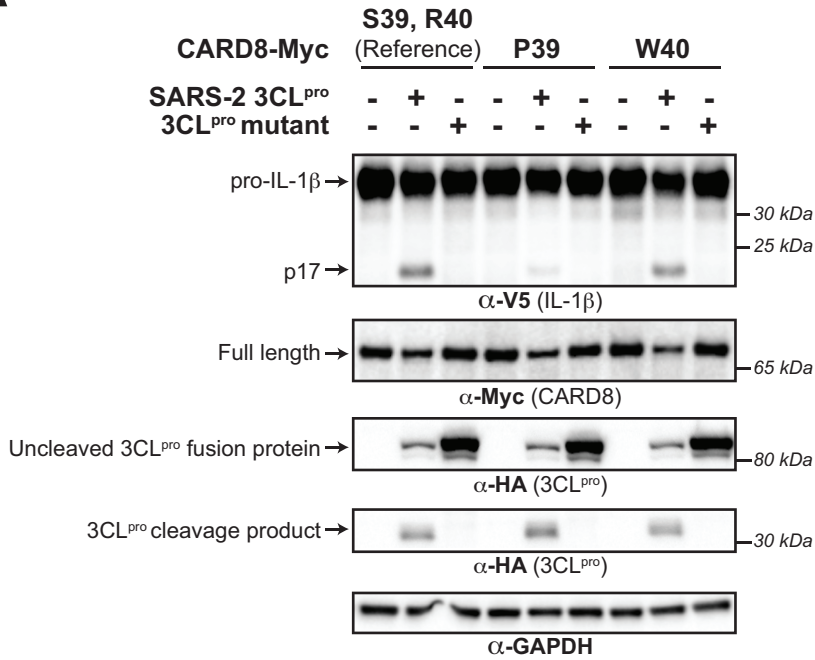an non-synonymous single nucleotide polymorphism (SNP) that encode CARD8 P39 and W40 are shown. Differences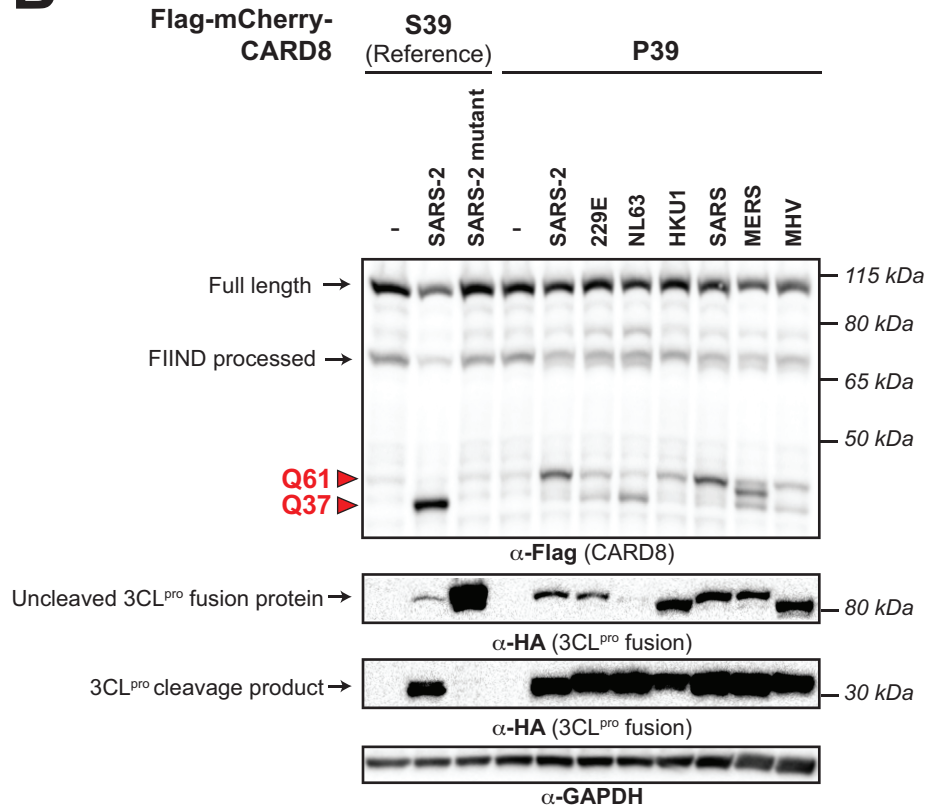 relative to the human reference protein sequence (accession NP_001338711) are indicated in red font. Coronavirus 3CL^{pro} (Q37 and Q61; red arrows) and HIV-1^{pro} cleavages sites in CARD8 are shown. '-' = indel.

A

B

784

785 **S10 Fig. The human CARD8 S39P variant has reduced sensitivity to coronavirus 3CL^{pro}**
786 **cleavage and inflammasome activation.**
787 (A) CARD8 inflammasome activation assay, where inflammasome activation is measured by
788 CASP1-dependent processing of pro-IL-1β to p17. *CARD8* knockout HEK293T cells were co-
789 transfected with Myc-tagged constructs encoding the reference allele of human CARD8 (protein
790 accession NP_001338711, mRNA accession NM_001351782.2) or the human CARD8 non-
791 synonymous single nucleotide polymorphism (SNP) CARD8-P39 (rs12463023) or CARD8-W40
792 (rs138177358) variants and the HA-tagged SARS-CoV-2 (SARS-2) 3CL^{pro}. (B) Comparison of
793 CARD8 S39 and CARD8 P39 cleavage by diverse coronavirus 3CL^{pros}. *CARD8* knockout
794 HEK293T cells were co-transfected using the indicated Flag-tagged mCherry-CARD8 fusion
795 constructs with HA-tagged protease constructs (empty vector ('-'), SARS-2 catalytically inactive
796 mutant (3CL^{pro} mutant) or active 3CL^{pro} from SARS-2, 229E, NL63, HKU1, SARS, MERS, or
797 MHV. Red triangles indicate cleavage sites 3CL^{pro}.
798

799

Consensus 3C^{pro} cleavage site
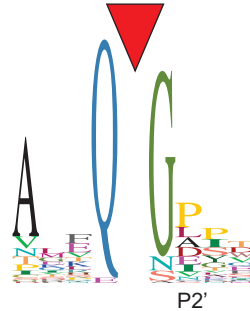
Human reference (S39)....IRLQ GSRK....   not detected

SNP rs12463023 (P39)....IRLQ G**P**RK....   **0.00108**

800

S11 Fig. A human SNP is predicted to result in a CARD8 protein that is cleavable by picornavirus 3C^{pros}.

A previously generated 3C^{pro} consensus cleavage motif for enteroviruses (a genus within picornaviruses), in which a proline is most common in the P2' position, is shown (*11*). Using this motif to search the human reference CARD8 protein sequence, which contains a serine at residue 39 (S39), does not generate a predicted cleavage site at Q37. However, a human SNP (rs12463023) results in a proline at residue 39 (P39), which generates a predicted 3C^{pro} cleavage site.

48

809
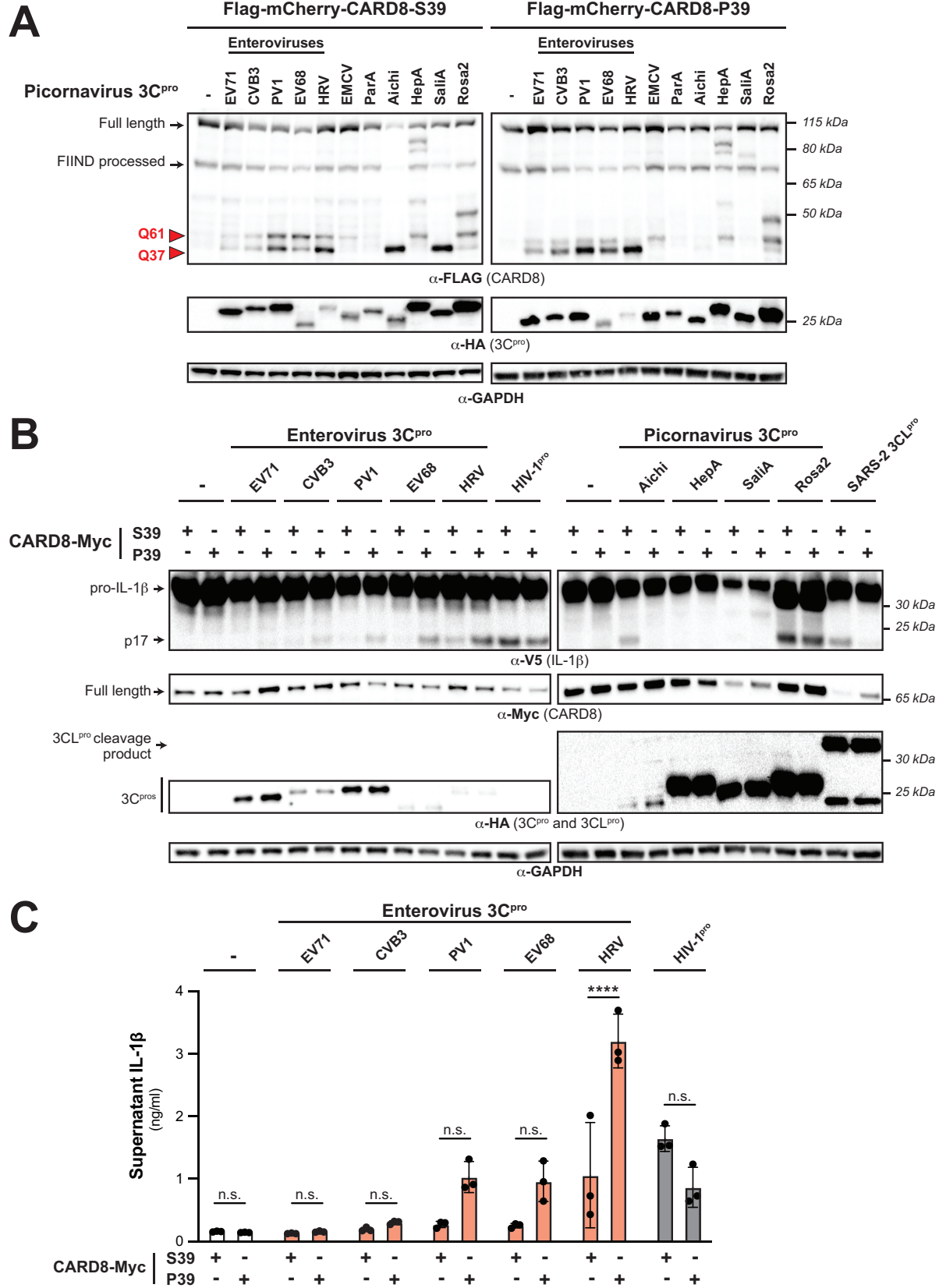
810 **S12 Fig. The CARD8 P39 variant is variably susceptible to picornavirus 3C^{pros}.**

811 (A) WT HEK293T cells were co-transfected using the indicated Flag-tagged mCherry-CARD8

812 fusion plasmid constructs with V5-IL-1β, CASP1, and HA-tagged 3C^{pro} constructs or empty

813 vector ('-'). 3C^{pros} from the following viruses were used: enterovirus A71 (EV71),

814 coxsackievirus B3 (CVB3), poliovirus 1 (PV1), enterovirus D68 (EV68), human rhinovirus A

815 (HRV), encephalomyocarditis virus (EMCV), human parechovirus A (ParA), Aichi virus

816 (Aichi), hepatitis A virus (HepA), human salivirus A (SaliA), and human rosavirus 2 (Rosa2).

817 Red arrows denote CARD8 fragments resulting from 3C^{pro} cleavage at indicated sites. (B)

818 CARD8 inflammasome activation assay, where inflammasome activation is measured by

819 CASP1-dependent processing of pro-IL-1β to p17. CARD8 knockout HEK293T cells were co-

820 transfected with Myc-tagged constructs encoding the reference allele of human CARD8 (protein

821 accession NP_001338711, mRNA accession NM_001351782.2) or the human CARD8 non-

822 synonymous single nucleotide polymorphism (SNP) CARD8-P39 (rs12463023) and the

823 indicated 3C^{pro}, 3CL^{pro}, or HIV-1^{pro} constructs, or empty vector ('-'). (C) IL-1β assay, which

824 measures the release of bioactive IL-1β in the culture supernatant of cells transfected as

825 described in (B). Individual values (n=3), averages, and standard deviations shown are

826 representative of experiments performed in triplicate. Data were analyzed using one-way

827 ANOVA with Tukey's post-test. n.s. = not significant. **** = $p<0.0001$.

828

50

829   **S1 Table. VIPR and RefSeq betacoronaviral polyproteins with 3CL cleavage site**
830   **concatenations.**

831   **S2 Table. Betacoronaviral polyproteins with unique 8mer 3CL cleavage site**
832   **concatenations.**

833   **S3 Table. Accession numbers of CARD8 sequences used for evolutionarily analyses.**

834   **S4 Table. Codon positions in full length CARD8 from hominoids and Old World monkeys**
835   **predicted to be evolving under recurrent positive selection by PAML, FUBAR, and FEL**
836   **analyses.**

837   **S5 Table. CARD8 missense variants (>100 allele counts) mapped to GRCh38 reported in**
838   **gnomAD v3.1.2.**

839   **S6 Table. CARD8 missense variants (>100 allele counts) mapped to GRCh38 reported in**
840   **gnomAD v3.1.2 represented by population with the highest allele frequency.**

841   **S7 Table. Primers, gBlocks, Twist fragments, and sgRNA.**

842   **S8 Table. List of antibody specifications.**